and 235 MeV that are used in the NCCE, Japan, the fitting parameters $\alpha_1$, $\beta_1$, $\alpha_2$, $\beta_2$, and $\gamma_2$ were calculated and are shown in Table I. Second, by the expansion of Eq. (4), $\sigma^2_{\text{comp,PBA}}(z)$ is extended

$$\sigma^2_{\text{comp,PBA}}(z) = \begin{cases} \sigma^2_{\text{comp,PBA}}(0) + \left\{2z \cdot \left(\frac{t}{2} + \text{airgap}\right) + z^2\right\} \cdot \sigma_\theta^2 & (0 < z \le d_{\text{smp}}) \\ \sigma^2_{\text{comp,PBA}}(d_{\text{smp}}) + \left\{2(z - d_{\text{smp}}) \cdot \left(\frac{t}{2} + \text{airgap} + d_{\text{smp}}\right) + (z - d_{\text{smp}})^2\right\} \cdot \sigma_\theta^2 & (z > d_{\text{smp}}) \end{cases}$$
$$= \sigma_0^2 + \sigma^2_{\text{comp,SR}_n}(z), \tag{A3}$$

where the first term $\sigma_0^2$ represents the spatial spread at the sampling depth $z = 0$ or $d_{\text{smp}}$, which corresponds to $\sigma_{\text{comp, PBA}}(0)$ or $\sigma_{\text{comp, PBA}}(d_{\text{smp}})$, respectively. Only the second term $\sigma^2_{\text{comp,SR}_n}(z)$ depends on the depth that is deeper than the sampling depth. Therefore, the spatial spread due to scattering of the range compensator in this technique is given as follows:

$$\sigma^2_{\text{comp,SR}_n}(z) = \begin{cases} \left\{2z \cdot \left(\frac{t}{2} + \text{airgap}\right) + z^2\right\} \cdot \sigma_\theta^2 & (0 < z \le d_{\text{smp}}) \\ \left\{2\left(z - d_{\text{smp}}\right) \cdot \left(\frac{t}{2} + \text{airgap} + d_{\text{smp}}\right) + \left(z - d_{\text{smp}}\right)^2\right\} \cdot \sigma_\theta^2 & (z > d_{\text{smp}}). \end{cases} \tag{A4}$$

Finally, the third component of $\sigma_{\text{pt, SR}}$ with respect to the multiple scattering within the patient[4] is calculated as follows:

$$\sigma^2_{pt,\text{SR}_n}(z) = \begin{cases} \sigma^2_{\text{pt,PBA}}(z,\ R_{\text{res}}(0)) & (0 < z \le d_{\text{smp}}), \\ \sigma^2_{\text{pt,PBA}}(z - d_{\text{smp}},\ R_{\text{res}}(d_{\text{smp}})) & (z > d_{\text{smp}}), \end{cases} \tag{A5}$$

where $\sigma_{pt,\,PBA}$, which is modeled as a function of the distance and the residual range in the one-dimensional scaling approximation, is the multiple scattering within the patient.[3] $R_{\text{res}}(0)$ and $R_{\text{res}}(d_{\text{smp}})$ are the residual ranges at depth = 0 and $d_{\text{smp}}$, respectively. $\sigma_{\text{pt,SR}_n}$ is also infinitesimally small at the depth $z = \text{d}z$ or $d_{\text{smp}} + \text{d}z$. For example, the beam size $\sigma_{PBA}$ and $\sigma_{\text{SR}_n}$ in depth in water are displayed in Fig. 8. The calculations were performed for energy typical in proton radiation therapy, that is, 190 MeV. The effective source size was set to 22.7 mm in agreement with the nozzle at NCCE. It was located at above 2745 mm from the isocenter, namely, 2645 mm from $z = 0$ plane. A 30-mm-thick flat range compensator was inserted in the beam line, which corresponds to $\sigma_\theta$ of 17.4 mmrad. The airgap between the compensator and the patient surface was chosen as 100 mm. $\sigma_{\text{PBA}}$ is equal to 2.3 mm at a depth of $z = 0$.

## APPENDIX B: CALCULATION OF FLUENCE AND DOSE DISTRIBUTIONS

In this Appendix, we summarize the calculation of the fluence and dose distributions. At the surface $(x,y,0)$, the fluence of the pencil beam per residual range $[\Phi(x, y; z = 0)]_R$ is represented as follows:

TABLE I. Fitting parameters for determination of the correction factors $h$(airgap) and $g(\sigma_{\text{size}})$.

| | $h$(airgap) | | $g(\sigma_{\text{size}})$ | | |
|---|---|---|---|---|---|
| Nominal energy (MeV) | $\alpha_1$ | $\beta_1$ | $\alpha_2$ | $\beta_2$ | $\gamma_2$ |
| 150 | 1.9894 | 70.062 | 0.840 | −129.18 | 4115.1 |
| 190 | 2.1370 | 68.486 | 3.2176 | −301.79 | 7393.7 |
| 235 | 2.2654 | 76.587 | 9.4454 | −699.28 | 14676 |

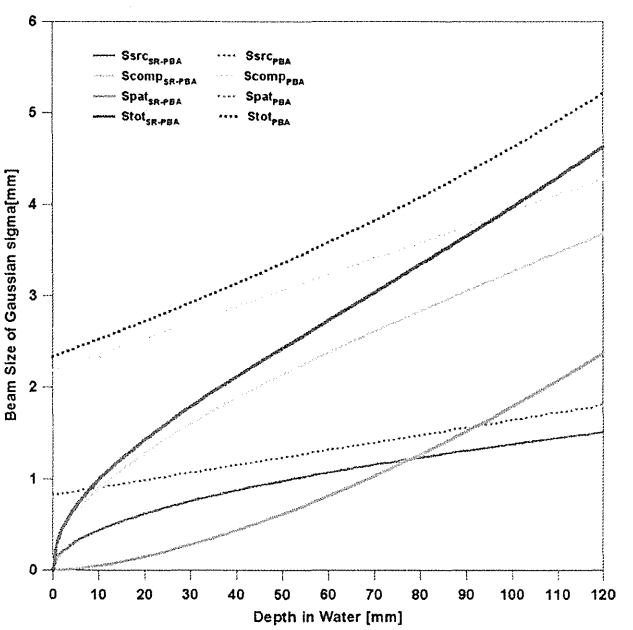


FIG. 8. Example of relationship between depth in water and beam size of Gaussian-sigma at the surface, when the 190 MeV mono-energetic proton beam is used. Thickness of range compensator is 30 mm and air-gap between the aperture and surface is 100 mm. Dotted and solid lines represent the beam size in the PBA and in the PBA with the spatial resampling, respectively. $S_{\text{src}}$, $S_{\text{comp}}$ and $S_{\text{pat}}$ lines show the beam size components due to the effective source size, scattering of the range compensator and multiple scattering within the patient, respectively. $S_{\text{pat-SRPBA}}$ overlaps $S_{\text{pat-PBA}}$. $S_{\text{tot}}$ represent the overall Gaussian-sigma.

$$[\Phi(x, y; z=0)]_g = \sum_{y'}\sum_{x'} \Delta x'\Delta y' \frac{\Phi_0(x', y')}{S} \times \exp\left(-\frac{(x-x')^2+(y-y')^2}{2\left[\sigma_{\mathrm{PBA}}(x', y'; z=0)\right]^2}\right) \times H(v_{\mathrm{surf}} - \sqrt{(x-x')^2+(y-y')^2}) \cdot \delta_{m,n}$$

$$S = \Delta x \Delta y \sum_{x,y} \exp\left(-\frac{(x-x')^2+(y-y')^2}{2\left[\sigma_{\mathrm{PBA}}(x', y'; z=0)\right]^2}\right),$$

$$m = \left\lfloor \frac{R}{\Delta R} + 0.5 \right\rfloor, n = \left\lfloor \frac{R_{\mathrm{res}}(x', y'; 0)}{\Delta R} + 0.5 \right\rfloor, \quad \text{(A6)}$$

where $R_{\mathrm{res}}(x, y; z)$ represents the residual range of the beams at a depth of $z$, which contributes to the point of interest $(x,y)$. $H(a)$ is the step function, with $H(a \geq 0) = 1$ and $H(a < 0) = 0$, while $\Delta x$ (or $\Delta x'$) and $\Delta y$ (or $\Delta y'$) are the sizes of dose calculation grid in $x$ and $y$, respectively. $v_{\mathrm{surf}}$, the cutoff distance of pencil beam, is defined as $3\sigma_{\mathrm{PBA}}(x', y'; 0)$. $\delta_{m,n}$ is Kronecker delta. $\lfloor a \rfloor$ is the floor function, which gives the largest integer that is smaller than $a$. Since the pencil beam is much smaller than the beam interval close to the sampling plane, the usual normalization factor $2\pi\sigma^2$ has to be substituted by $S$. This normalization guarantees that the numerical integral dose in each slice is correct. When the spatial resampling procedure is additionally implemented at a depth of $z = d_{\mathrm{smp}}$, the fluence per residual range on the sampling plane $d_{\mathrm{smp}}$ is written as follows:

$$[\Phi(x, y; z=d_{\mathrm{smp}})]_R = \sum_{y'}\sum_{x'} \Delta x'\Delta y' \frac{[\Phi(x', y'; z=0)]_R}{S} \times \exp\left(-\frac{(x-x')^2+(y-y')^2}{2\left[\sigma_{\mathrm{SR}_n}(x', y'; d_{\mathrm{smp}})\right]^2}\right) \times H(v_{\mathrm{smp}} - \sqrt{(x-x')^2+(y-y')^2}) \cdot \delta_{m,n}$$

$$S = \Delta x \Delta y \sum_{x,y} \exp\left(-\frac{(x-x')^2+(y-y')^2}{2[\sigma_{\mathrm{SR}_n}(x', y'; z=d_{\mathrm{smp}})]^2}\right),$$

$$m = \left\lfloor \frac{R}{\Delta R} + 0.5 \right\rfloor, n = \left\lfloor \frac{R_{\mathrm{res}}(x', y'; d_{\mathrm{smp}})}{\Delta R} + 0.5 \right\rfloor, \quad \text{(A7)}$$

where $v_{\mathrm{smp}}$, the cutoff distance of sub-beam, is defined as $3\sigma_{\mathrm{SR}}(x', y'; d_{\mathrm{smp}})$. Consequently, from Eqs. (A6) and (A7), the dose at the point of interest $(x, y, z)$ being deposited by sub-beams is given as follows:

$$D_{\mathrm{SR}}(x, y, z) = \sum_{R'=0}^{R_0}\sum_{y'}\sum_{x'} \Delta x'\Delta y' [\Phi(x', y'; z=0 \text{ or } d_{\mathrm{smp}})]_{R'} \times \frac{C(x', y', WEL(x', y', z))}{S} \times \exp\left(-\frac{(x-x')^2+(y-y')^2}{2\left[\sigma_{\mathrm{SR}_n}(x', y'; z)\right]^2}\right)$$

$$S = \Delta x \Delta y \sum_{x,y} \exp\left(-\frac{(x-x')^2+(y-y')^2}{2\left[\sigma_{\mathrm{SR}_n}(x', y'; z)\right]^2}\right). \quad \text{(A8)}$$

## APPENDIX C: APPLICATION OF THE SPATIAL RESAMPLING TECHNIQUE FOR A HEAD AND NECK TUMOR

To show the potential of the SRPBA to improve the accuracy of dosimetric calculations to the PBA, the spatial resampling technique was implemented for the pencil-beam calculation for a head and neck tumor with a volume of approximately 130 $\mathrm{cm}^3$ from three gantry angles. We used the mono-energetic proton beam because it clarifies the improvement of the pencil-beam dose calculation. With the spatial resampling technique, an isocenter was chosen as a secondary resampling depth $d_{\mathrm{smp}}$. The total dose distributions were normalized at the isocenter. The smearing distance of the range compensator[25] was taken at 4.5 mm. We monitored the minimum and maximum subtraction doses and the computing time. Figure 9 depicts the dose distributions in an axial plane obtained using (a) the PBA, (b) the PBA with resampling only at $z = 0$ minus the one without resampling, and (c) the PBA with resampling at $z = 0$ and $z = d_{\mathrm{smp}}$ minus the one without resampling In the figures, over/underestimations of dose regions were observed especially around the nasal sinus. The number of elemental pencil beams was 3581 in all algorithms on average. Minimum and maximum subtraction doses relative to the isocenter dose were (a) −15.1% and 9.70%, and (b) −17.9%

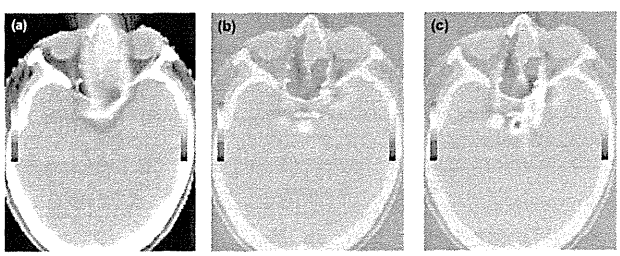


FIG. 9. Dose distributions in the axial plane of the patient with a head and neck tumor using (a) the PBA, (b) the PBA with resampling at $z = 0$ minus the PBA, and (c) the PBA with resampling at $z = 0$ and $z = d_{\mathrm{smp}}$ minus the PBA. Color bars are associated with dose values (×0.1% relative to the isocenter dose).

and 13.8%, respectively. The increases in computing time were factors of (a) 8.5 and (b) 20.

[a]Author to whom correspondence should be addressed. Electronic mail: egashira@nuclear.jp; Telephone: +81-3-5861-2958; Fax: +81-3-5861-2958.

[1]K. R Hogstrom, M. D. Michael, and P. R. Almond, "Electron beam dose calculations," Phys. Med. Biol. **26**, 446–460 (1981).

[2]P. L. Petti, "Differential-pencil-beam dose calculations for charged particles," Med. Phys. **19**, 137–149 (1992).

[3]L. Hong, M. Gotein, M. Buccuilini, R. Comiskey, B. Gottschalk, S. Rosenthal, C. Serago, and M. Urie, "Pencil beam algorithm for proton dose calculations," Phys. Med. Biol. **41**, 1305–1330 (1996).

[4]H. Szymanowski, A. Mazal, C. Nauaye, S. Biensan, R. Ferrand, M. C. Murillo, S. Caneva, G. Gaboriaud, and J. C. Rosenwald, "Experimental determination and verification of the parameters used in a proton pencil beam algorithm," Med. Phys. **28**, 975–987 (2001).

[5]B. Schaffner, E. Pedroni, and A. Lomax, "Dose calculation models for proton treatment planning using a dynamic beam delivery system: An attempt to include density heterogeneity effects in the analytical dose calculation," Phys. Med. Biol. **44**, 27–41 (1999).

[6]B. Schaffner, "Proton dose calculation based on in-air fluence measurements," Phys. Med. Biol. **53**, 1545–1562 (2008).

[7]N. Kanematsu, M. Komori, S. Yonai, and A. Ishizaki, "Dynamic splitting of Gaussian pencil beams in heterogeneity-correction algorithms for radiotherapy with heavy charged particles," Phys. Med. Biol. **54**, 2015–2027 (2009).

[8]N. Kanematsu, "Modeling of beam customization devices in the pencil-beam splitting algorithm for heavy charged particle radiotherapy," Phys. Med. Biol. **56**, 1361–1371 (2011).

[9]H. Szymanoqski and U. Oelfke, "Two-dimensional pencil beam scaling: An improved proton dose algorithm for heterogeneous media," Phys. Med. Biol. **47**, 3313–3330 (2002).

[10]L. Eyges, "Multiple scattering with energy loss," Phys. Rev. **74**, 1534–1535 (1948).

[11]A. S. Shiu and K. R. Hogstrom, "Pencil-beam redefinition algorithm for electron dose distributions," Med. Phys. **18**, 7–18 (1991).

[12]R. A. Boyd, K. R. Hogstrom, and G. Starkschall, "Electron pencil-beam redefinition algorithm dose calculations in the presence of heterogeneities" Med. Phys. **28**, 2096–2104 (2001).

[13]N. Kanematsu, S. Yonai, A. Ishizaki, and M. Torikoshi, "Computational modeling of beam-customization devices for heavy-charged-particle radiotherapy," Phys. Med. Biol. **53**, 3113–3127 (2008).

[14]V. L. Highland, "Some practical remarks on multiple scattering," Nucl. Instrum. Methods **129**, 497–499 (1975).

[15]V. L. Highland, "Some practical remarks on multiple scattering," Nucl. Instrum. Methods **161**, 171 (1979) (Erratum).

[16]T. Bortfeld and W. Schlegel, "An analytical approximation of depth-dose distribution for therapeutic proton beams," Phys. Med. Biol. **41**, 1331–1339 (1996).

[17]T. Nishio, "Present status and planning of facilities for proton and heavy ion cancer treatment in Japan—National Cancer Center," J. At. Energy Soc. **41** 1134–1138 (1999).

[18]T. Tachikawa, T. Sato, T. Ogino, and T. Nishio, "Proton beam therapy facilities of the National Cancer Center East Hospital," Radiat. Indust. **84**, 48–53 (1999).

[19]T. Nishio, S. Kataoka, M. Tachibana, K. Matsumura, N. Uzawa, H. Saito, T. Sasano, M. Yamaguchi, and T. Ogino, "Development of a simple control system for uniform proton dose distribution in a dual-ring double scattering method." Phys. Med. Biol. **51**, 1249–1260 (2006).

[20]E. Spezi, A. L. Angelini, F. Romani, and A. Ferri, "Characterization of a 2D ion chamber array for the verification of radiotherapy treatments," Phys. Med. Biol. **50**, 3361–3373 (2005).

[21]K. Hotta, R. Kohno, Y. Takada, Y. Hara, R. Tansho, T. Himukai, S. Kameoka, T. Matsuura, T. Nishio, and T. Ogino, "Improved dose-calculation accuracy in proton treatment planning using a simplified Monte Carlo method verified with three-dimensional measurements in an anthropomorphic phantom," Phys. Med. Biol. **55**, 3545–3556 (2010).

[22]R. Kohno, Y. Takada, T. Sakae, T. Terunuma, K. Matsumoto, A. Nohtomi, and H. Matsuda, "Experimental evaluation of validity of simplified Monte Carlo method in proton dose calculations," Phys. Med. Biol. **48**, 1277–1288 (2003).

[23]M. Goitein, "A technique for calculating the influence of thin inhomogeneities on charged particle beams," Med. Phys. **5**, 258–264 (1978).

[24]U. Schneider, B. Schaffner, T. Lomax, E. Pedroni, and A. Tourovsky, "A technique for calculating range spectra of charged particle beams distal to thick inhomogeneities," Med. Phys. **25**, 457–463 (1998).

[25]M. Urie, M. Goitein, and M. Wagner, "Compensating for heterogeneities in proton radiotherapy," Phys. Med. Biol. **29**, 533–566 (1984).

# Development of activity pencil beam algorithm using measured distribution data of positron emitter nuclei generated by proton irradiation of targets containing $^{12}C$, $^{16}O$, and $^{40}Ca$ nuclei in preparation of clinical application

Aya Miyatake[a)]
*Keen Medical Physics Services, 2-11-8 yayoi, Bunkyo-ku, Tokyo 113-0032, Japan*

Teiji Nishio and Takashi Ogino
*Particle Therapy Division, Research Center for Innovative Oncology, National Cancer Center, Kashiwa, 6-5-1 Kashiwano-ha, Kashiwa-shi, Chiba 277-8577, Japan*

(Received 1 April 2011; revised 10 August 2011; accepted for publication 31 August 2011; published 27 September 2011)

**Purpose:** The purpose of this study is to develop a new calculation algorithm that is satisfactory in terms of the requirements for both accuracy and calculation time for a simulation of imaging of the proton-irradiated volume in a patient body in clinical proton therapy.
**Methods:** The activity pencil beam algorithm (APB algorithm), which is a new technique to apply the pencil beam algorithm generally used for proton dose calculations in proton therapy to the calculation of activity distributions, was developed as a calculation algorithm of the activity distributions formed by positron emitter nuclei generated from target nuclear fragment reactions. In the APB algorithm, activity distributions are calculated using an activity pencil beam kernel. In addition, the activity pencil beam kernel is constructed using measured activity distributions in the depth direction and calculations in the lateral direction. $^{12}C$, $^{16}O$, and $^{40}Ca$ nuclei were determined as the major target nuclei that constitute a human body that are of relevance for calculation of activity distributions. In this study, "virtual positron emitter nuclei" was defined as the integral yield of various positron emitter nuclei generated from each target nucleus by target nuclear fragment reactions with irradiated proton beam. Compounds, namely, polyethylene, water (including some gelatin) and calcium oxide, which contain plenty of the target nuclei, were irradiated using a proton beam. In addition, depth activity distributions of virtual positron emitter nuclei generated in each compound from target nuclear fragment reactions were measured using a beam ON-LINE PET system mounted a rotating gantry port (BOLPs-RGp). The measured activity distributions depend on depth or, in other words, energy. The irradiated proton beam energies were 138, 179, and 223 MeV, and measurement time was about 5 h until the measured activity reached the background level. Furthermore, the activity pencil beam data were made using the activity pencil beam kernel, which was composed of the measured depth data and the lateral data including multiple Coulomb scattering approximated by the Gaussian function, and were used for calculating activity distributions.
**Results:** The data of measured depth activity distributions for every target nucleus by proton beam energy were obtained using BOLPs-RGp. The form of the depth activity distribution was verified, and the data were made in consideration of the time-dependent change of the form. Time dependence of an activity distribution form could be represented by two half-lives. Gaussian form of the lateral distribution of the activity pencil beam kernel was decided by the effect of multiple Coulomb scattering. Thus, the data of activity pencil beam involving time dependence could be obtained in this study.
**Conclusions:** The simulation of imaging of the proton-irradiated volume in a patient body using target nuclear fragment reactions was feasible with the developed APB algorithm taking time dependence into account. With the use of the APB algorithm, it was suggested that a system of simulation of activity distributions that has levels of both accuracy and calculation time appropriate for clinical use can be constructed. 
[DOI: 10.1118/1.3641829]

Key words: proton therapy, proton beam monitoring, simulation of activity distribution, activity pencil beam algorithm, beam ON-LINE PET system, target nuclear fragment reaction

## I. INTRODUCTION

The Beam ON-LINE PET system mounted on a rotating gantry port (BOLPs-RGp) was previously developed, and proton therapy has been performed for all patients with measurement using BOLPs-RGp at the National Cancer Center, Kashiwa, since October, 2007.[1] This system measures annihilation gamma rays generated from the irradiated volume in

a patient body from the start of proton beam irradiation to 200 s after the end of irradiation using BOLPs-RGp. Up to now, the number of cases measured is about 150, such as cases involving head and neck, prostate, liver, lung, and brain. Furthermore, an apparatus for viewing and analysis, which exclusively uses the data measured by BOLPs-RGp, has been developed and used.[2] Study involving analysis of irradiated body tissues of patients using clinical data has been reported,[1,2] which proved that the use of BOLPs-RGp in clinical proton therapy is very useful for quality assurance and control and provides improvement in terms of accuracy.

Research in the monitoring of the proton-irradiated volume via nucleus activation has been worked on.[1–17] To verify the absolute accuracy of planned dose distributions using measured activity distributions, we have to simulate activity distributions from dose distributions. Research on the simulation of activity distributions has been carried out. One of the methods is calculation of activity distributions using a Monte Carlo simulation, in which data of cross sections for the rate of target nuclear fragment reactions between proton and nuclei compositing patients' bodies are used with GEANT4 and FLUKA.[18–20] And, in carbon ion therapy it is reported that a technique of activity simulation utilizes the database of Monte Carlo calculated activity distribution which is formed in $^{12}C$ pencil beam irradiation of PMMA targets.[21] That research group deals with both projectile and target nuclear fragmentation reactions but only target nuclear fragments are treated in this study. It is difficult to determine the value of cross sections as the value is dependent on proton energy and the species of positron emitter nuclei that are generated. At present, the reported data of cross sections are not sufficient for simulation of activity distributions in terms of quantity and accuracy.[22] However, determination of the value of cross sections is now underway in other groups, and it may be expected that data of cross sections that are sufficient for simulation will be obtained. Therefore, it can be said that the calculation accuracy of simulation based on a detailed physics process using a Monte Carlo simulation will likely improve with a corresponding increased accuracy in the knowledge of reaction cross sections in the near future.

To use the simulation in clinical therapy, the calculation time is one of the necessary conditions in addition to the calculation accuracy. Because an enormous amount of data is essential for calculation using the Monte Carlo simulation, which is a statistical calculation method with random numbers, it takes hours to obtain the result of calculation. Although there are methods, like lookup table, e.g., phase-space file, to improve the speed of simulation such as GEANT and FLUKA, it may be difficult to adopt the simulation system using the Monte Carlo simulation for an on-site location near a clinical therapy where it is now needed for treatment of a lot of patients. However, since BOLPs-RGp is now used in clinical therapy, there are ongoing efforts of constructing a simulation system that meets the requirements in terms of both accuracy and calculation time for clinical use. It is necessary to develop a new calculation algorithm that can be used in clinical therapy to provide improvements in proton therapy using BOLPs-RGp.

The purpose of this study is to develop a new calculation algorithm for the simulation system of imaging of activity distributions corresponding to the planned irradiation volume in clinical proton therapy.

## II. MATERIAL AND METHOD

### II.A. The new calculation algorithm of activity distributions proposed in this study

The necessary conditions of the calculation algorithm of activity distributions are high speed and high accuracy in calculation for utilization of the simulation system for imaging of activity distributions in clinical proton therapy. The new algorithm was developed using activity pencil beam kernel for calculation of activity distributions in this study. The data of measured depth activity distributions and calculated lateral activity distributions are used for obtaining the activity pencil beam data.

#### *II.A.1. Depth activity distribution*

A quantity of positron emitter nuclei generated from target nuclear fragment reactions is affected by each value of the cross section for the reactions within the range of energy used for proton therapy. Since the accuracy of the value regarding the cross section has a direct effect on the accuracy of the simulation, the determined value for the cross section is very important in the simulation of activity distributions. However, it cannot be said that the data of the cross section required for simulation calculation are sufficient in terms of accuracy and quantity at present. The phantom study using PET/CT imaging suggested the potential of millimeter accuracy in proton therapy.[16] But in patient study, it was reported that the accuracy of a simulation that calculated activity distributions in a patient body was within 30% by uncertainties of cross section, washout effects, and stoichiometric composition in patient body.[15]

Therefore, improvements in the accuracy of values regarding the cross sections of target nuclear fragment reactions are needed to use the simulation of activity distributions to image the planned and proton-irradiated volume with high accuracy in clinical proton therapy. In this study, "virtual positron emitter nuclei ($^{12}C_{virtual}$, $^{16}O_{virtual}$, and $^{40}Ca_{virtual}$)" was defined as the nuclei merged of various positron emitter nuclei generated from each target nucleus by target nuclear fragment reactions with irradiated proton beam (see Eq. (1)).

$$\begin{aligned} &^{12}C(p,x)^{11}C,^{10}C, \text{etc.} \rightarrow ^{12}C(p,x)^{12}C_{virtual}, \\ &^{16}O(p,x)^{15}O,^{14}O, \text{etc.} \rightarrow ^{16}O(p,x)^{16}O_{virtual}, \\ &^{40}Ca(p,x)^{39}Ca,^{38}Ca, \text{etc.} \rightarrow ^{40}Ca(p,x)^{40}Ca_{virtual}. \end{aligned} \quad (1)$$

A new approach was adopted that uses measured activity distributions of virtual positron emitter nuclei when the proton beam irradiates a compound containing target nuclei, not which uses values of reaction cross section determined one by one for each reaction channel. The data of measured activity distributions of virtual positron emitter nuclei that we obtained

in this study cover the information of the most relevant reaction channels generating positron emitter nuclei in irradiation targets. Moreover, decrease of energy and attenuation of incident proton flux occur at the depth point in thick targets. A similar attenuate phenomenon occurs in a patient body irradiated by proton beam. Therefore, the data are significant for this study in view of future application to describe the nuclear fragmentation reactions occurring in the human body. In the calculation of activity distributions, measured data of depth activity distributions can improve the accuracy of calculation.

#### *II.A.2. Calculation algorithm of activity distributions for simulation of imaging of planned irradiation volume by proton beam: activity pencil beam algorithm (APB algorithm)*

The accuracy of calculation using the Monte Carlo simulation is affected by statistical error, which depends on the total number of histories. Calculation must be performed with a sufficiently large number of histories to meet the accuracy required in each case. With the Monte Carlo simulation, it takes hours to obtain the result of calculation with the accuracy required for clinical use. A simulation with calculation time within several minutes is demanded for proton therapy of many patients in hospital.

For simulation system of imaging of activity distributions in daily proton therapy, the activity pencil beam algorithm (APB algorithm) was developed as a new calculation algorithm with both accuracy and high speed. The pencil beam algorithm is a standard algorithm of dose calculation in proton therapy. This algorithm is a technique for calculation that considers depth dose distributions along the direction that the proton beam travels, and that also approximates lateral dose distributions of the Gaussian form at every depth point by effect of multiple Coulomb scattering. However, effect of the scattering by inhomogeneous density in material from axis of beam direction is not considered in the pencil beam algorithm. Therefore, the accuracy of calculation of dose distributions deteriorates in areas of a steep density gradient, such as lungs, bone, and nasal cavity. Although the accuracy of calculation using pencil beam algorithm may deteriorate in a site of a patient's body, the algorithm is generally used for dose calculation in clinical proton therapy because it is well balanced between accuracy and calculation time required in clinical use. These considerations are similar in APB algorithm for the calculation of activity distributions formed by target nuclear fragment reactions between proton and nuclei compositing a human body.

In APB algorithm, depth and lateral activity distributions are defined by measurement of activity of $^{12}C_{virtual}$, $^{16}O_{virtual}$ and $^{40}Ca_{virtual}$ nuclei and calculation of multiple Coulomb scattering. The activity pencil beam kernel, $A_{mono}(X_{virtual}; r, z, t_{ag})$, is shown in Eq. (2) as following:

$$A_{mono}\left(X_{virtual}; r, z, t_{ag}\right) = A_{meas.}\left(X_{vitrual}; z, t_{ag}\right) \cdot \frac{1}{2 \cdot \pi \cdot \sigma_r(z)^2} \cdot \exp\left(-\frac{r^2}{2 \cdot \sigma_r(z)^2}\right),$$
$$\left\{X_{vitrual} = {}^{12}C_{vitrual}, {}^{16}O_{vitrual}, {}^{40}Ca_{vitrual}\right\}. \quad (2)$$

Here, $A_{meas.}\left(X_{virtual}; r, z, t_{ag}\right)$ is measured depth activity distribution, $X_{virtual}$ virtual positron emitter nuclei, $r$ lateral position from axis of beam direction, $z$ depth point in water equivalent material, $t_{ag}$ time after generated virtual positron emitter nuclei, and $\sigma_r$ the parameter of lateral distribution decided by effect of multiple Coulomb scattering. There are various techniques to decide parameter of $\sigma_r$.[23–26] If APB algorithm is adopted, it can be estimated that the calculation time will be several minutes because activity calculation time is similar to dose calculation time using pencil beam algorithm theoretically. Therefore, the calculation time required in clinical use will be satisfied.

### II.B. Beam ON-LINE PET system mounted on a rotating gantry port: BOLPs-RGp

The beam ON-LINE PET system mounted on a rotating gantry port (BOLPs-RGp) installed on the proton beam line in our treatment room in the National Cancer Center, Kashiwa, was developed for proton beam monitoring and is used in clinical proton therapy.[1] The opposing detector heads of planar type with a high position resolution were composed of BGO crystals with a crystal size of $2 \times 2 \times 20$ mm$^3$. The field of view (FOV) at the iso-center was $164.8 \times 167.0$ mm$^2$. The center of its detection area corresponded with the iso-center under a condition where the detectors were opposite each other on a rotating gantry port. The opposing detectors rotated together with the rotating gantry. The detector heads opposite each other were installed along the axis of the proton beam direction and an area in the range direction of the proton beam can be observed. A PET image is reconstructed using a maximum likelihood algorithm taking into consideration the attenuation coefficient of 511-keV gamma rays in the patient's body calculated using the patient's planning CT image data. The distance between the opposing detector heads can be adjusted from 30 to 100 cm.

With regard to the performance of this detection system, the maximum collection rate of the data for the coincident detection was about 1 Mcps. The position resolution of measuring activity was about 2 mm of the full width at half maximum (FWHM) at the iso-center in the FOV in an experiment using a $^{22}$Na point source. The detection efficiency was calibrated using a thin-flat acrylic container filled with $^{18}$F solution at each distance between detector heads from 30 to 100 cm. In addition, the viewer of activity for clinical analysis (VACA; TR Japan), which is a display and analysis tool for the data detected by BOLPs-RGp, was developed and used.[2]

### II.C. Measurement of depth activity distributions

#### *II.C.1. Irradiation target for measurements of activity*

The main nuclei of which human body tissue is composed and which cause target nuclear fragment reactions with proton are the following: $^{12}$C, $^{14}$N, $^{16}$O and $^{40}$Ca, in the range of proton beam energy used in proton therapy (i.e., 0–250 MeV). Important nuclei for imaging of irradiated volume in a patient's body are $^{12}$C, $^{16}$O, and $^{40}$Ca nuclei by the ratio of

the four nuclei in a human body tissue and the data of a reaction cross section for target nuclear fragment reactions in the range of proton beam energy used in proton therapy.[2] Therefore, $^{12}C$ nuclei and $^{16}O$ nuclei, as well as $^{40}Ca$ nuclei, were selected as the target nuclei, and activity distributions of virtual positron emitter nuclear formed from a reaction between proton and the target nuclei were obtained.

Polyethylene (PE: $CH_2$) and water were the irradiated targets, and activity distributions that originated from a reaction between proton and $^{12}C$ nuclei or $^{16}O$ nuclei were measured. In the experiment using the two targets of PE and water, hydrogen nuclei have no part in the target nuclear fragment reactions. Consequently, the results of measurement for the two targets are equal to the results of reaction for $^{12}C$ nuclei and $^{16}O$ nuclei with proton. The target of PE was made of polyethylene with a high density of 0.96 g/cm$^3$. By addition of a little gelatin (the mass of the gelatin was 1.95% the mass of water) to pure water, a target of water with no flow was made. Because handling of solid calcium is difficult, packed powder of calcium oxide (CaO), which can be handled comparatively easily in a container made of PE, was the target of $^{40}Ca$ nuclei. The results of measurement of CaO target included the reaction of proton and $^{40}Ca$ nuclei as well as $^{16}O$ nuclei. Then, results of only the reaction of $^{40}Ca$ nuclei and proton were obtained by subtracting the results of reaction of $^{16}O$ nuclei and proton from the results of CaO target. The difference of proton fluence calculated in CaO target and water target was about 5% around range point of 223 MeV proton beam. Result of activity distribution of $^{40}Ca_{virtual}$ nuclei was considered by the difference of proton flux attenuation in CaO and water targets.

Considering the detecting area of BOLPs-RGp and the size of the proton beam, the size of PE target was $8 \times 8 \times 12$ cm$^3$. Targets of water and CaO were the containers made of PE with a thickness of 5 mm, filled with the water including a little gelatin or the powdered CaO, and the inside volume of the containers was $8 \times 8 \times 12$ cm$^3$ (see Fig. 1). To acquire the depth activity distributions produced by $^{40}Ca$ nuclei and proton nuclei, the number of irradiated proton to target was normalized using activity value of 5-mm thickness wall on the side of the beam entrance in container of PE for water ($H_2O$) and CaO targets. In experiment of range measurement after passing through the target by the proton beam, the water equivalent length of 1 cm PE and CaO were 1.02 cm and 1.15 cm, respectively.

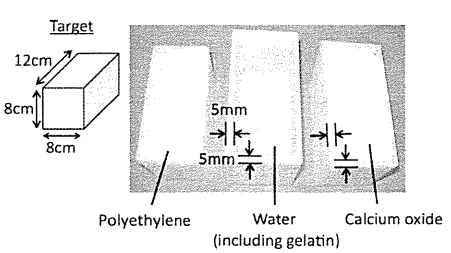


FIG. 1. Targets consisted of the target nuclei, that is, $^{12}C$, $^{16}O$, and $^{40}Ca$. The left is polyethylene, the middle is water including gelatin, and the right is calcium oxide.

### II.C.2. Proton beam irradiations to target

Each target was irradiated using mono-energetic proton beams with energies of 223, 179, and 138 MeV. The irradiated dose was equivalent to 15 Gy at around the Bragg Peak to reduce the statistical error of measurement activity of virtual positron emitter nuclei in irradiation target. The proton beam of 2 cm in diameter at the iso-center was irradiated in 2–20 s. Each target was measured on the condition that intensity of proton beams in each measurement and irradiation time in the same energy was constant.

$^{40}Ca_{virtual}$ nuclei include positron emitter nuclei with short half-lives around 1 s, such as $^{38}Ca$ nuclei and $^{39}Ca$ nuclei. Therefore, an additional measurement such that the time of proton beam irradiated to CaO target was less than 1 s was done. The activity measurement was performed twice for each proton beam energy in order to measure the generated positron emitter nuclei of short half-lives with improved statistics.

### II.C.3. Measurement of depth activity distributions using BOLPs-RGp

The depth activity distribution of virtual positron emitter nuclei generated by proton beam irradiation in a target was measured using BOLPs-RGp. The irradiation target was set up at the position where the center of the target corresponded to the iso-center (see left side of Fig. 2). The distance between the opposing detector heads of PET was 90 cm and the gantry angle was 270°. The measurement time was 303.3 min (5 h 3 min and 20 s) in one irradiation for each target for obtaining enough characteristic of virtual positron emitter nuclei generated by proton beam irradiation. The output of measurement values occurred every second from the start of measurement to 200 s and, after 200 s, an integrated count for every 10 s was output. For the CaO target, an additional measurement of 200 s was performed. The output of measurement values occurred every second for measurement of virtual positron emitter nuclei with short half-lives generated by proton irradiation.

The FOV of BOLPs-RGp was about 16 cm; however, the proton beam range in water was about 14–30 cm at 138–223 MeV. The area was so small that measurement could not be finished in a single session. Therefore, the whole measurement area of the target was divided in the depth direction, and each separate measurement area was measured gradually. The measurement area was shown in right side of Fig. 2. The numbers of separate areas were five at 223 MeV, three at 179 MeV, and two at 138 MeV. The depicted proton dose distributions were measured using water phantom. The depth of the dose distribution shows water equivalent length (WEL). The method of gradual measurement involved the measurement area being moved by changing the thickness of a fine degrader, which adjusted the beam range, and inserting the PE material with homogeneous thickness into the place at which the patient's bolus was put. Measured depth activity

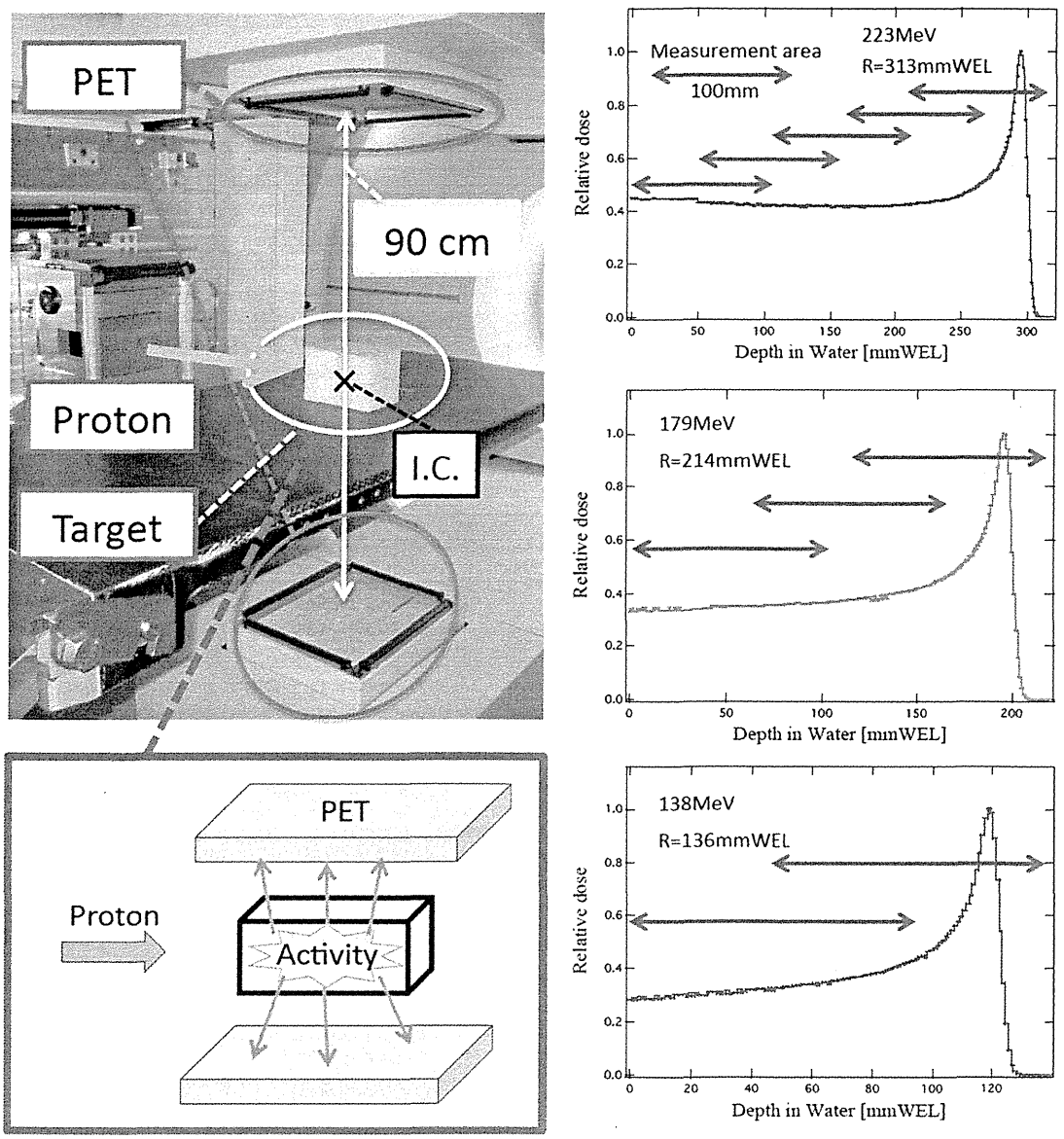


FIG. 2. The design of a system to measure activity distributions (left) and measurement area of the target each energy (right) using BOLPs-RGp in NCC, Kashiwa.

distributions for every energy and target were acquired by connecting each measured activity distribution gradually.

### II.D. Making of activity pencil beam kernel using the measured activity distributions

The pencil beam algorithm takes into consideration both depth activity distributions along the direction toward the center axis of proton beam travel and lateral activity distribution at depth by effect of multiple Coulomb scattering. In the direction of the center axis of the proton beam, water length equivalent to the length of each calculation grid was calculated, and this calculated length was given a one-dimensional value of percent depth activity (PDA). The effect of multiple Coulomb scattering was included to lateral activity distribution with Gaussian form similarly to proton dose calculation by pencil beam algorithm. The formula

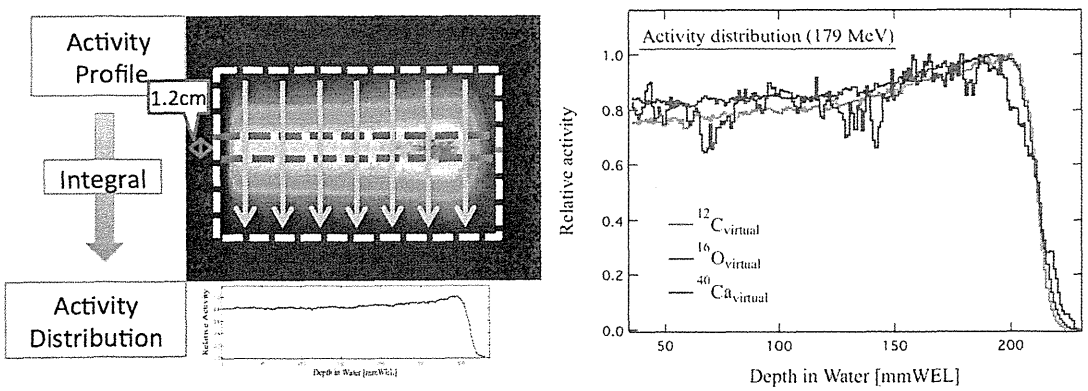


FIG. 3. The approach for making activity distributions from integrated measured two-dimensional activity profile (left). The measured depth activity distributions of virtual positron emitter nuclei that were obtained by irradiating proton beam of 179 MeV to every target nucleus (right).

proposed by Lynch was used for the activity pencil beam kernel in this study.[25]

## III. RESULTS AND DISCUSSION

### III.A. Results of measured depth activity distributions

The profile of a target activity obtained using BOLPs-RGp is two-dimensional information, which is taken in two perpendicular directions to the opposing detectors of PET installed on BOLPs-RGp. As shown to the left of Fig. 3, first, the measured two-dimensional activity profile was integrated in the direction perpendicular to the beam axis. Second, divided measured data were revised, such as by normalizing the number of incident proton, and the revised data were gathered and connected. This was the case for the results of measured depth activity distributions for every energy and target. Figure 3 shows the measured depth activity distributions obtained by irradiating proton beam of 179 MeV for every target nucleus. In terms of the distribution of $^{40}Ca_{virtual}$ nuclei, it can be seen that the dispersion of $^{40}Ca_{virtual}$ nuclei distribution is greater than that of the other two nuclei. This can be explained by there being statistical dispersion in $^{40}Ca_{virtual}$ nuclei data because $^{40}Ca_{virtual}$ nuclei data are obtained by subtracting $^{16}O_{virtual}$ nuclei data from the CaO data. The dispersion could be reduced by increasing the measurement time and the number of measurement data.

### III.B. Verification of the form and the time dependence of depth activity distributions

#### *III.B.1. Depth activity distributions by starting time of measurement after proton beam irradiation*

Activity distribution is based on the information of virtual positron emitter nuclei generated by target nuclear fragment reactions. The quantity of activity detected by BOLPs-RGp is dependent on the time of irradiation and detection because positron emitter nuclei have half-lives that differ for every kind of nucleus. Therefore, it is necessary to verify the time dependence of the form of a measured activity distribution during the measurement period. The irradiation time of a proton beam varies for each patient and treatment by the difference of fractional dose or whether irradiation with synchronized respiration was carried out. Change of depth activity distribution by period of proton irradiation was verified and estimated by the measured activity data using BOLPs-RGp in clinical treatment.[1,2]

About five areas of depth activity distributions of $^{12}C_{virtual}$ nuclei obtained using a proton beam of 223 MeV irradiating PE targets were verified. Figure 4 is measurement results of depth activity distributions by starting time of measurement after 223 MeV proton beam irradiation to PE target. Two activity distributions ((a) and (b)) shown in the figure are measured in the area around entrance of PE target with incident proton beam and the proton beam range of 223 MeV. The measured depth activity distribution data of 100 s was analyzed by the time from irradiation to starting BOLPs-RGp measurement, *Ts*, of 0 (immediately after the irradiation), 0.5, 1, 2, 3, 5, 7, and 10 min. In the area around entrance of PE target with incident proton beam of 223 MeV, the change of the form of depth activity distributions to the change of *Ts* was within ±10% [Fig. 4(a)]. In the deepest area around the beam range, although the forms of six depth activity distributions with *Ts* greater than 1 min were similar, the forms of distributions about *Ts*= and 0.5 were greatly different from others [Fig. 4(b)]. In these circumstances, it was clear that the form of depth activity distributions changed with the depth and the irradiation time.

Depth activity distributions of $^{12}C_{virtual}$ nuclei obtained by proton beam irradiation to PE are the function of the time and the depth, which were expressed by two elements: $^{10}C$ nucleus whose half-life is about 20 s and $^{11}C$ nucleus whose half-life is about 20 min. $^{10}C$ nuclei with a short half-life are included in activity data measured immediately after proton beam irradiation. As time passed, a difference in the form of the depth activity distribution occurred because mainly information on $^{11}C$ nuclei became available. Therefore, it can be considered that the reason why the form of the depth activity distribution changed is that the ratio of the amount of information about $^{10}C$ nuclei and $^{11}C$ nuclei in the measured data changed with time from the end of irradiation to the start of the measurement (i.e., *Ts*).

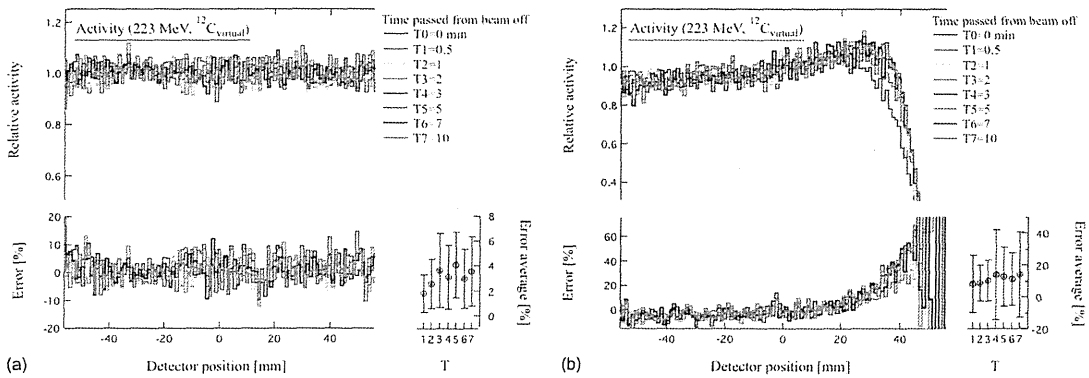


FIG. 4. Depth activity distributions of $^{12}C_{virtual}$ nuclei by starting time of measurement after 223 MeV proton beam irradiation to PE target are shown. (a) The area around entrance of PE target with incident proton beam and (b) the area around the proton beam range of 223 MeV. The lower right-hand graph showed the average error and deviation to data of T0 ($Ts = 0$).

As for the activity distribution around the beam range in Fig. 4(b), it can be observed that the range of the depth activity distribution at $Ts = 0$ is shallower than the other six distributions with $Ts$ greater than 1 min. One neutron is generated by the reaction to generate a $^{11}C$ nucleus, and two neutrons are generated by the reaction to generate a $^{10}C$ nucleus in the target fragment reaction between $^{12}C$ nuclei and proton. The reaction to generate a $^{10}C$ nucleus needs more proton energy to generate a neutron than the reaction to generate a $^{11}C$ nucleus. Therefore, it can be considered that the range of depth activity distributions formed mainly from the information of $^{10}C$ nuclei was shallower than the distributions of the others. Moreover, it was observed that there was hardly a difference in depth activity distributions for $Ts$ greater than 1 min. This may suggest that the quantitative proportion of generated $^{10}C$ nuclei to $^{12}C_{virtual}$ nuclei was small.

### III.B.2. Half-lives of virtual positron emitter nuclei ($^{12}C_{virtual}$, $^{16}O_{virtual}$, and $^{40}Ca_{virtual}$)

It turned out that the simulation of activity distributions had to take the time dependence of the form of depth activity distributions into consideration given the result of Sec. III B 1 above. Therefore, the change of activity-intensity at each depth point with the passage of time was analyzed for the measured activity distributions for every target nucleus. The decay curves of measured activity data during the period of measurement (about 5 h) in a very small volume, which was set up around the depth point in the target, were obtained and the characteristics of the decay curves were identified. 10–16 points for analysis were set up and all targets and energies were analyzed in consideration of the form of the measured activity distribution. Figure 5 shows the result about $^{12}C_{virtual}$ nuclei by irradiation of 223 MeV proton beam.

The virtual positron emitter nuclei generated by proton irradiation were roughly divided into two elements by the length of the nucleus half-life for all the target nuclei in this study. The two kinds of nuclei whose half-lives are 20 min ($^{11}C$ nucleus) and 20 s ($^{10}C$ nucleus) are generated from $^{12}C$ nuclei as target nuclei, in the same way, 10–20 min ($^{11}C$ and $^{13}N$ nuclei) and several minutes or under ($^{15}O$, $^{14}O$, and $^{10}C$ nuclei) are done from $^{16}O$ nuclei and under 1 s ($^{38}Ca$ and $^{39}Ca$ nuclei) and several minutes ($^{38}K$ nuclei) are done from $^{40}Ca$ nuclei. Therefore, the decay curves of measured activity data in small volumes, which were set up for every depth point for analysis using Eq. (3) constructed with elements separated into two groups of half-lives, were approximated.

$$N_{act.}(z,t) = A_{T_{long}}(z) \cdot \left(\frac{1}{2}\right)^{\frac{t}{T_{long}(z)}} + A_{T_{short}}(z) \cdot \left(\frac{1}{2}\right)^{\frac{t}{T_{short}(z)}}. \quad (3)$$

Here, $N_{act.}$ represents measured activity data, $t$ measurement time, $T_{long}$ and $T_{short}$ half-lives, and $A_{T_{long}}$ and $A_{T_{long}}$ total measured activity of each half-life. $N_{act}$ is total measured activity at $t = 0$. Figure 5 shows the decay curves that were obtained from measured activity data of $^{12}C_{virtual}$ nuclei using 223 MeV proton beam and the fitting curves at 10

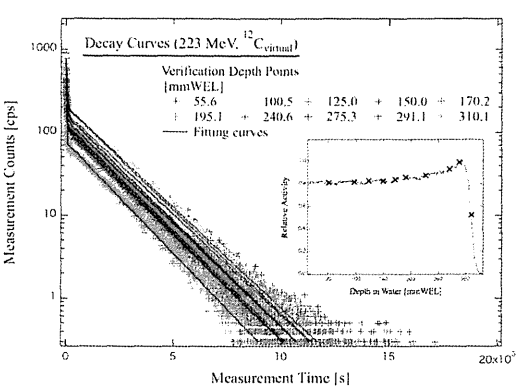


FIG. 5. The decay curves of measured activity data of $^{12}C_{virtual}$ nuclei during the measurement period (about 5 h) and the curves approximated using Eq. (3) in a very small volume at each depth point (223 MeV, PE target).

TABLE I. The results of approximation with two elements for each target and energy to the depth.

| Target | Energy [MeV] | $R_{T_{long}}(\pm\Delta R_{T_{long}})$ | $T_{long}(\pm\Delta T_{long})$ [s] | $\Delta R_{T_{long}}/R_{T_{long}}$ [%] | $\Delta T_{long}/T_{long}$ [%] |
|---|---|---|---|---|---|
| $^{12}$C | 223 | 0.274 (±0.030) | 1201 (±30) | 10.8 | 2.5 |
| | 179 | 0.313 (±0.073) | 1215 (±12) | 23.4 | 1.0 |
| | 138 | 0.337 (±0.085) | 1208 (±8) | 25.2 | 0.7 |
| $^{16}$O | 223 | 0.029 (±0.011) | 1354 (±339) | 38.4 | 25.1 |
| | 179 | 0.030 (±0.007) | 1257 (±74) | 22.4 | 5.9 |
| | 138 | 0.036 (±0.011) | 1078 (±69) | 29.6 | 6.4 |
| $^{40}$Ca | 223 | 0.003 (±0.001) | 582 (±84) | 28.7 | 14.4 |
| | 179 | 0.002 (±0.000) | 631 (±57) | 24.7 | 9.1 |
| | 138 | 0.002 (±0.001) | 576 (±36) | 23.0 | 6.2 |
| Target | Energy [MeV] | $R_{T_{short}}(\pm\Delta R_{T_{short}})$ | $T_{short}(\pm\Delta T_{short})$ [s] | $\Delta R_{T_{short}}/R_{T_{short}}$ [%] | $\Delta T_{short}/T_{short}$ [%] |
| $^{12}$C | 223 | 0.726 (±0.030) | 20 (±3) | 4.1 | 14.2 |
| | 179 | 0.687 (±0.073) | 20 (±1) | 10.7 | 3.5 |
| | 138 | 0.663 (±0.085) | 19 (±1) | 12.8 | 3.3 |
| $^{16}$O | 223 | 0.971 (±0.011) | 139 (±6) | 1.2 | 4.6 |
| | 179 | 0.970 (±0.007) | 132 (±2) | 0.7 | 1.5 |
| | 138 | 0.964 (±0.011) | 126 (±2) | 1.1 | 1.3 |
| $^{40}$Ca | 223 | 0.997 (±0.001) | 1 (±0) | 0.1 | 13.0 |
| | 179 | 0.998 (±0.000) | 1 (±0) | 0.0 | 7.0 |
| | 138 | 0.998 (±0.001) | 1 (±0) | 0.1 | 7.1 |

depth points. Fitting results of decay curves for each target and energy at the depth points were summarized in Table I.

The elements with short half-lives were approximated with higher accuracy than the elements with long half-lives in terms of both half-lives and ratios of these elements in the decay curves obtained from the measured activity data. Probably, the virtual positron emitter nuclei with short half-life had greater influence on the quantity of activity originating from virtual positron emitter nuclei, which might be detected immediately after proton irradiation (that is, $N_{act.}(z, t = 0)$), than the virtual positron emitter nuclei with a long half-life. Table I suggests that the activity distributions obtained immediately after proton irradiation were formed by the activity that originated from virtual positron emitter nuclei with short half-lives mainly for all targets and energies. About 30% of activity distributions of $^{12}C_{virtual}$ nuclei were contributed to by the activity of virtual positron emitter nuclei with long half-lives, and the contributions to activity distributions of $^{16}O_{virtual}$ nuclei and activity distributions of $^{40}Ca_{virtual}$ nuclei were only a few percent.

The kinds of nuclei that contributed to measured activity data could be inferred from the approximated half-lives shown in Table I. $T_{long}$ and $T_{short}$ were about 20 min and 20 s for the approximate results of measured activity data of $^{12}C_{virtual}$ nuclei, respectively, which suggested the existence of $^{11}$C nuclei and $^{10}$C nuclei. From $T_{long}$ being around 20 min, the measured activity data of $^{16}O_{virtual}$ nuclei might have mainly been contributed to by $^{11}$C nuclei and various generated positron emitter nuclei such as $^{13}$N nuclei (half-life: about 10 min). In addition, from $T_{short}$ being around 130 s, it was estimated that many $^{15}$O nuclei and a few other nuclei contributed to the measured activity data of $^{16}O_{virtual}$ nuclei. As for the results of $^{40}Ca_{virtual}$ nuclei, the existence of $^{38}$K nuclei (half-life: about 8 min) was suggested from $T_{long}$ being about 10 min and that of $^{38}$Ca nuclei (half-life: 0.45 s) and $^{39}$Ca nuclei (half-life: 0.86 s) from $T_{short}$ being 1 s. The nuclei whose half-lives were under 1 s, such as $^{38}$Ca nuclei and $^{39}$Ca nuclei, were both approximated as one nuclei whose half-life was 1 s because the output of the measurement using BOLPs-RGp was every 1 s. In these circumstances, it is easy to distinguish the nuclei with short half-lives from the virtual positron emitter nuclei because half-lives of the generated positron emitter nuclei, which were classified as the virtual positron emitter nuclei with short half-lives, were especially short. It could be considered that the approximate accuracy of the elements with short half-lives was high for the reasons stated above.

Figure 6 shows plots of parameter, $A_{T_{long}}, A_{T_{short}}$, $T_{long}, T_{short}$, calculated using Eq. (3) for each target nucleus at 179 MeV proton beam. The activity ratios of $^{12}C_{virtual}$, $^{16}O_{virtual}$, and $^{40}Ca_{virtual}$ nuclei were calculated using Eq. (4)

$$R_{T_{long},T_{short}}(\mathrm{X_{virtual}};z) \equiv \frac{A_{T_{long},T_{short}}(\mathrm{X_{virtual}})}{N_{act.}(z,t=0)} = \begin{cases} a(\mathrm{X_{virtual}}) + \dfrac{b(\mathrm{X_{virtual}})}{1+\left(\dfrac{c(\mathrm{X_{virtual}})}{z}\right)^{k(\mathrm{X_{virtual}})}}, & (\mathrm{X_{virtual}}=^{12}\mathrm{C_{virtual}}) \\ a(\mathrm{X_{virtual}}) + b(\mathrm{X_{virtual}})\cdot z^{k(\mathrm{X_{virtual}})}, & (\mathrm{X_{virtual}}=^{16}\mathrm{O_{virtual}}) \\ a(\mathrm{X_{virtual}}). & (\mathrm{X_{virtual}}=^{40}\mathrm{Ca_{virtual}}) \end{cases} \quad (4)$$

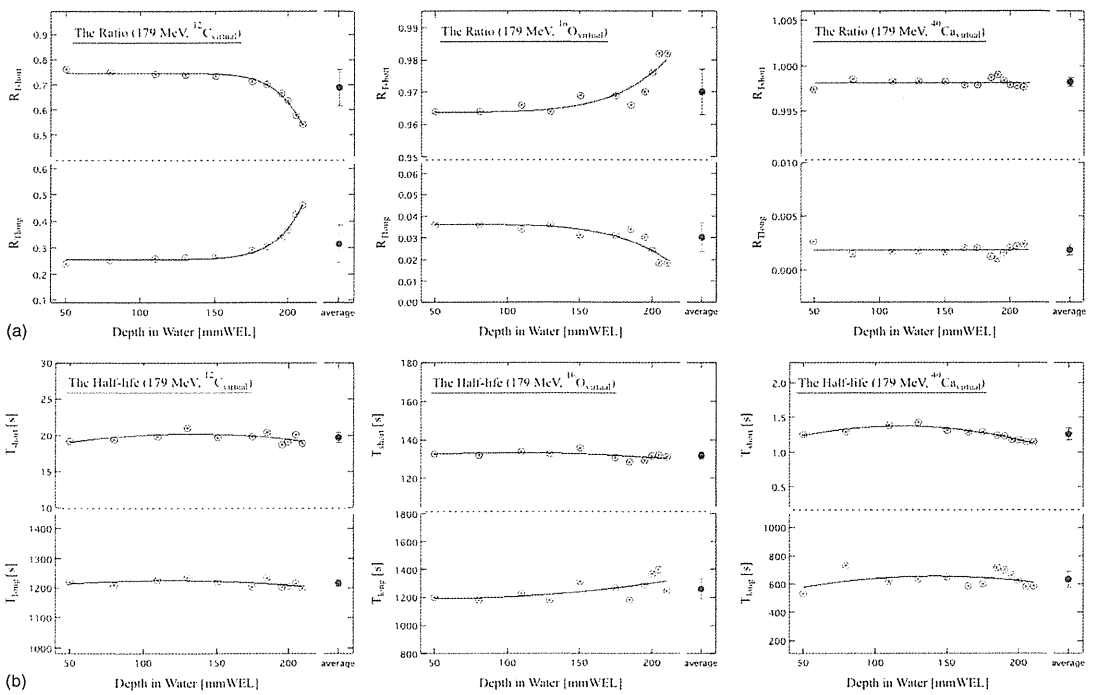


FIG. 6. The plotted points were the results that were the ratio of each half-life group of elements (a) and the hail-lives (b) approximated using Eq. (3) for each virtual positron emitter nuclei at 179 MeV. The curves approximated the results of approximation using Eqs. (4) and (5).

Here, $R_{T_{long},T_{short}}$ is the ratio of $X_{virtual}$ nucleus with each half-life element, and $a, b, c, k$ are free parameters for fitting of data in each equation. The measured activity distributions of $^{40}Ca_{virtual}$ nuclei were mainly formed by the elements of short half-lives according to the result of ratio of $^{40}Ca$ nuclei half-life elements (see Table I). The half-lives both long and short were calculated using Eq. (5) for each virtual positron emitter nuclei.

$$T_{long,short}(X_{virtual}; z) = a(X_{virtual}) + b(X_{virtual}) \cdot z + c(X_{virtual}) \cdot z^2. \quad (5)$$

Here, $T_{long,short}$ is each half-life of $X_{virtual}$ nucleus. Table II shows the fitting results for each target and energy. The values that were obtained from measured activity data were widely distributed because the analysis volume was set up as small as possible to verify the depth dependence. This could explain why the points that were the results of that analysis are diffusely spread in Fig. 6. Therefore, the change of the form of depth activity distributions with the depth dependence was considered by using of the Eqs. (4) and (5) decided by the results of each target nucleus in this study.

Three nuclei, $^{12}C$, $^{16}O$, and $^{40}Ca$, were proposed to be the main components related to the imaging of proton-irradiated volume in a patient body in this study. It was found that the elements with a short half-life for each target nucleus mainly affected the activity distributions of virtual positron emitter nuclei obtained by proton irradiation to all target nuclei. In other words, it was suggested that the activity distributions obtained by proton irradiation of human body tissues, which were regarded as being mainly composed of $^{12}C$ nuclei, $^{16}O$ nuclei, and $^{40}Ca$ nuclei, were approximated by three half-life elements. It was reported that the activity distributions obtained by proton irradiation of human body tissues in clinical therapy could be approximated by three half-life elements, as found in our previous study.[2] It could be said that the results of this study to analyze three target nuclei ($^{12}C$, $^{16}O$, and $^{40}Ca$) have a strong relationship to the results of the previous study on clinical data.

### III.C. Activity pencil beam kernel using measured depth activity distributions

Activity pencil beam kernel was constructed by the measured depth activity distribution data of virtual positron emitter nuclei and calculated lateral distributions of Gauss form considering the effect of multiple Coulomb scattering. The measured depth activity distribution data included the influence of time and depth dependence. Form of activity pencil beam kernel was decided by each energy of incident proton beam and each nucleus of $^{12}C$, $^{16}O$, and $^{40}Ca$. And, the data were prepared for installing the simulation system of activity distributions. Figure 7 shows calculation results of the activity pencil beam kernel of $^{12}C_{virtual}$, $^{16}O_{virtual}$, and $^{40}Ca_{virtual}$ nuclei with mono-energetic proton beam of 179 MeV. There

TABLE II. The results of approximation using Eqs. (4) and (5) for each target and energy.

| | | $R_{T_{long}}$ | | | |
|---|---|---|---|---|---|
| Target | Energy [MeV] | $a$ | $b$ | $c$ | $k$ |
| $^{12}C$ | 223 | 0.262 | 0.124 | 301.3 | 33.9 |
| | 179 | 0.255 | 2.757 | 258.0 | 12.2 |
| | 138 | 0.274 | 3.471 | 185.1 | 8.3 |
| | | $a$ | $b$ | $k$ | |
| $^{16}O$ | 223 | 0.040 | 0.000 | 5.1 | |
| | 179 | 0.036 | 0.000 | 5.8 | |
| | 138 | 0.044 | 0.000 | 5.9 | |
| | | Constant Value | | | |
| $^{40}Ca$ | 223 | 0.003 | | | |
| | 179 | 0.002 | | | |
| | 138 | 0.002 | | | |
| | | $R_{T_{short}}$ | | | |
| Target | Energy [MeV] | $a$ | $b$ | $c$ | $k$ |
| $^{12}C$ | 223 | 0.604 | 0.134 | 303.4 | −31.3 |
| | 179 | −0.888 | 1.633 | 244.8 | −12.6 |
| | 138 | −1.811 | 2.537 | 177.0 | −8.4 |
| | | $a$ | $b$ | $k$ | |
| $^{16}O$ | 223 | 0.960 | 0.000 | 5.1 | |
| | 179 | 0.964 | 0.000 | 5.8 | |
| | 138 | 0.956 | 0.000 | 5.9 | |
| | | Constant Value | | | |
| $^{40}Ca$ | 223 | 0.997 | | | |
| | 179 | 0.998 | | | |
| | 138 | 0.998 | | | |
| | | $T_{long}$ | | | |
| Target | Energy [MeV] | $a$ | $b$ | $c$ | |
| $^{12}C$ | 223 | 1194.5 | 0.448 | −0.002 | |
| | 179 | 1192.7 | 0.531 | −0.002 | |
| | 138 | 1216.8 | −0.308 | 0.002 | |
| $^{16}O$ | 223 | 1085.6 | 4.778 | −0.014 | |
| | 179 | 1210.5 | −0.588 | 0.005 | |
| | 138 | 1113.1 | −2.343 | 0.019 | |
| $^{40}Ca$ | 223 | 813.3 | −2.870 | 0.007 | |
| | 179 | 471.1 | 2.593 | −0.009 | |
| | 138 | 578.5 | 0.402 | −0.004 | |
| | | $T_{short}$ | | | |
| Target | Energy [MeV] | $a$ | $b$ | $c$ | |
| $^{12}C$ | 223 | 16.4 | 0.081 | 0.000 | |
| | 179 | 17.2 | 0.045 | 0.000 | |
| | 138 | 17.7 | 0.031 | 0.000 | |
| $^{16}O$ | 223 | 139.6 | 0.078 | 0.000 | |
| | 179 | 130.5 | 0.052 | 0.000 | |
| | 138 | 129.1 | −0.114 | 0.001 | |
| $^{40}Ca$ | 223 | 1.4 | 0.001 | 0.000 | |
| | 179 | 1.0 | 0.007 | 0.000 | |
| | 138 | 1.1 | 0.000 | 0.000 | |

are four graphs of depth activity distributions, coefficient of multiple Coulomb scattering to depth ($1\sigma$), two-dimensional activity pencil beam kernel, and depth activity distributions toward the distance from the central proton beam axis shown in Fig. 7.

The pencil beam algorithm takes into consideration the way in which the center of the proton beam passes through inhomogeneous material in calculation of proton dose distribution. However, lateral Gaussian distribution only represents the scatter in water with no density gap. The accuracy of calculation deteriorates at the point with a large density gap in the inhomogeneous area composed of matter with various densities, such as bone and air. The same phenomenon occurs in the APB algorithm. On the other hand, research to improve the accuracy of the pencil beam algorithm has been carried out worldwide. Calculation using the pencil beam algorithm is being developed to a higher level of accuracy. For instance, research is being carried out on the development of the calculation algorithm with high accuracy on the border of inhomogeneous matter by regarding a scattered beam after passing fine degrader and bolus as a thin beam.[27] The calculation accuracy of activity distributions using the APB algorithm is the same as the calculation accuracy of dose distributions in clinical proton therapy. Therefore, it is evaluated that the calculation accuracy using the APB algorithm satisfies the accuracy required in clinical use. With progress in the research and development on improving the accuracy of dose calculation, mainly using the pencil beam algorithm, it is certain that the accuracy of activity distribution calculation using the APB algorithm will also be improved. In these circumstances and given these future possibilities, it will be very valuable for calculation of activity distributions to utilize the pencil beam algorithm.

### III.D. Sorting CT image of patients into composite nuclear image in a human body for simulation of activity distributions

In proton dose calculation, the physical process of a proton beam passing into a human body is based on electromagnetic interaction, which is mainly proportional to the ionization potential of matter depended on the atomic number Z. In addition, the CT value of a CT image taken for the physical reactions of Photoelectric effect and Compton scattering between a human body and x-ray of about 100 kV depends on the electron density of matter depended on Z. Using these relationships with Z, proton dose distributions are calculated using CT image of patient for treatment planning in clinical proton therapy. On the other hand, target nuclear fragment reactions, which are nuclear reactions between atomic nuclei that constitute a human body and proton in proton therapy, are related to the atomic number Z and the mass number A, as an nucleus is identified by these factors of Z and A. Therefore, sorting the CT image of patients into nuclei is essential to simulate imaging of the planned irradiation volume, although it is suggested that calculation with high speed and high accuracy using APB algorithm can be used in a clinical routine. The best approach is

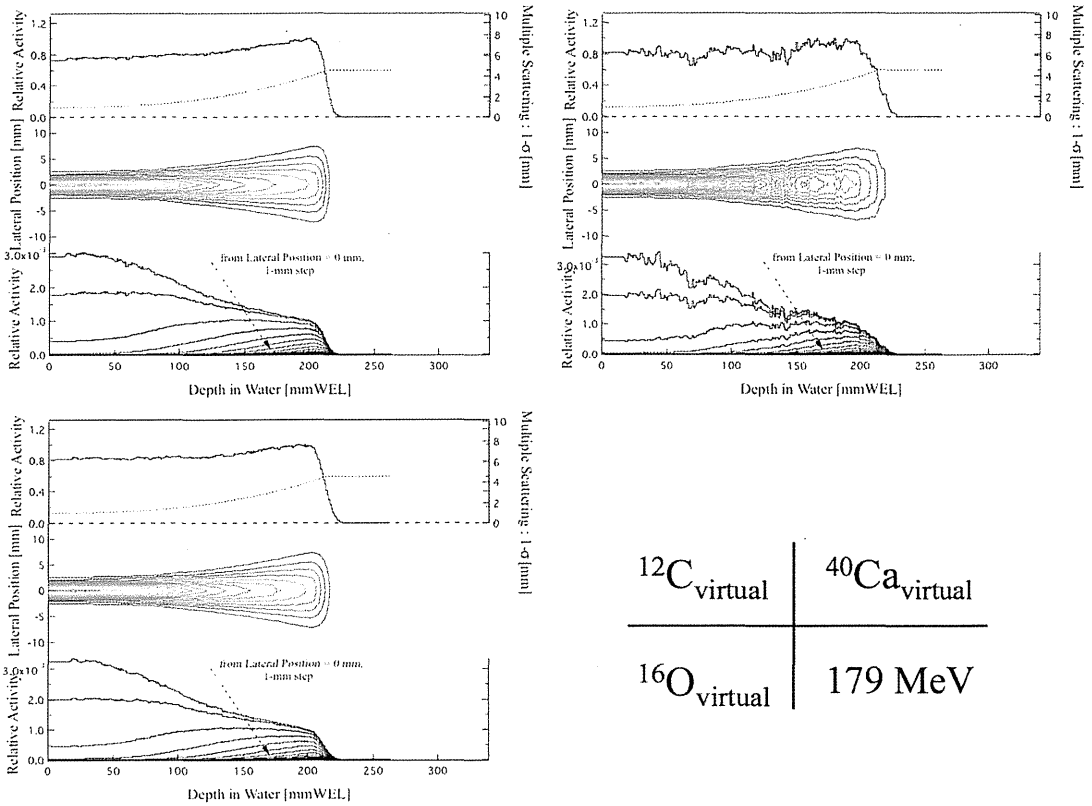


FIG. 7. The results of calculated activity pencil beam kernel of $^{12}C_{virtual}$, $^{16}O_{virtual}$, and $^{40}Ca_{virtual}$ nuclei with mono-energetic proton beam of 179 MeV. There are four graphs, the upper: depth activity distributions and coefficient of multiple Coulomb scattering to depth ($1\sigma$), the middle: two-dimensional activity pencil beam kernel, the lower: depth activity distributions toward the distance from the central proton beam axis.

that sorting of CT images into nuclei is done on an individual patient because the composition of human body tissue differs among individuals. However, such a technique has not been established yet. The accuracy of identifying human body tissue from CT values affects the accuracy of dose calculation in proton therapy.[28,29] Research on the relationship between CT value and human body tissue to improve the accuracy of dose and activity calculations in proton therapy has been continuously done.[15,16,29–33] The accuracy of identifying nuclei in the human body from CT images has a strong relationship to the accuracy of the whole simulation of imaging of the planned irradiation volume. Therefore, which technique of identification is to be chosen is an issue to be resolved.

## IV. CONCLUSIONS

The APB algorithm that has both the accuracy and the calculation time required for clinical use was developed as a new calculation algorithm for the simulation of activity distributions. It was expected that a simulation system with the APB algorithm for making activity distributions of irradiated volume in patient body using activity pencil beam kernel could be put into clinical use.

It was found that three target nuclei, $^{12}C$, $^{16}O$, and $^{40}Ca$, were important and appropriate for calculation of activity distributions by verification and analysis of clinical data in this study. In terms of the information of target nuclear fragment reactions between proton and nuclei in a human body required for calculation of activity distributions, the information of reactions was enriched with the measured data of the generated virtual positron emitter nuclei to improve the accuracy of simulation of activity distributions. Acquisition of the data of target nuclear fragment reactions between $^{40}Ca$ nuclei and proton within the range of energy used for proton therapy in this study was very useful because such data are limited at present. Moreover, high accurate proton therapy can be provided by the development of a new calculation algorithm considering the time and depth dependence of the forms of activity distributions.

We have been constructed a simulation system of imaging of proton-irradiated volume equipped the APB algorithm now. Then, it will be possible to verify the changes of the irradiated volume and the influence of washout effect on

images of activity distributions by comparing the results of calculation with measurement using BOLPs-RGp. It is thought that there are many seeds (e.g., *in vivo* dosimetry) of research based on measurement and calculation of activity in irradiated volume. The accuracy of activity distribution calculation using APB algorithm is future problem. Therefore, it will be important for verification of measured activity distribution using BOLPs-RGp and calculated activity distribution using APB algorithm in clinical cases. It is expected that the APB algorithm can be utilized for proton therapy with imaging of irradiated volume. We will be able to provide high quality proton therapy for patients.

## ACKNOWLEDGMENTS

The authors would like to thank T. Okamoto of Hamamatsu Photonics K. K., H. Oka and K. Tojima of MED-I Asia Japan, Ltd., for technical support. They also thank the staff members of the Proton Radiotherapy Department of National Cancer Center, Kashiwa, for their help, the members of SHI Accelerator Service, Ltd., and Accelerator Engineering, Inc., for the operation of the proton apparatus. This work was supported by Health and Labour Science Research Grants from the Japanese Government.

[a]Electronic mail: miyatake.keenmps@gmail.com

[1]T. Nishio, A. Miyatake, T. Ogino, K. Nakagawa, N. Saijo, and H. Esumi, "The development and clinical use of a beam ON-LINE PET system mounted on a rotating gantry port in proton therapy," Int. J. Radiat. Oncol., Biol., Phys. **76**, 277–286 (2010).

[2]A. Miyatake, T. Nishio, T. Ogino, N. Saijo, H. Esumi, and M. Uesaka, "Measurement and verification of positron emitter nuclei generated at each treatment site by target nuclear fragment reactions in proton therapy," Med. Phys. **37**, 4445–4455 (2010).

[3]G. W. Bennett, A. C. Goldberg, G. S. Levine, J. Guthy, and J. Balsamo, "Beam localization via 15O activation in proton-radiation therapy," Nucl. Instrum. Methods **125**, 333–338 (1975).

[4]U. Oelfke, G. Lam, and M. Atkins, "Proton dose monitoring with PET: Quantitative studies in Lucite," Phys. Med. Biol. **41**, 177–196 (1996).

[5]D. W. Litzenberg, D. A. Roberts, M. Y. Lee, K. Pham, A. M. Vander Molen, R. Ronningen, and F. D. Becchetti, "On-line monitoring of radiotherapy beams: Experimental results with proton beams," Med. Phys. **26**(6), 992–1006 (1999).

[6]T. Nishio, T. Ogino, M. Shimbo, S. Katsuta, S. Kawasaki, T. Murakami, T. Sato, Y. Kojima, K. Murakami, and H. Ikeda, "Distributions of $\beta^+$ decayed nucleus produced from the target fragment reaction in $(CH_2)n$ and patient liver targets by using a proton beam for therapy," *Abstracts of the XXXIV PTCOG MEETING in Boston*, p. 15–16 (2001).

[7]Y. Hishikawa, K. Kagawa, M. Murakami, H. Sasaki, T. Akagi, and M. Abe, "Usefulness of positron-emission tomographic images after proton therapy," Int. J. Radiat. Oncol., Biol., Phys. **53**, 1388–1391 (2002).

[8]W. Enghardt, P. Crespo, F. Fiedler, R. Hinz, K. Parodi, J. Pawelke, and F. Ponisch, "Dose quantification from in-beam positron emission tomography," Radiother. Oncol. **73**, Suppl. 2. S96–98 (2004).

[9]T. Nishio, T. Sato, H. Kitamura, K. Murakami, and T. Ogino, "Distributions of $\beta^+$ decayed nuclei generated in the $CH_2$ and $H_2O$ targets by the target nuclear fragment reaction using therapeutic MONO and SOBP proton beam," Med. Phys. **32**(4), 1070–1082 (2005).

[10]T. Nishio, T. Ogino, K. Nomura, and H. Uchida, "Dose-volume delivery guided proton therapy using beam ON-LINE PET system," Med. Phys. **33**(11), 4190–4197 (2006).

[11]T. Nishio, A. Miyatake, K. Inoue, S. Katsuta, T. Gomi-Miyagishi, R. Kohno, S. Kameoka, K. Nakagawa, and T. Ogino, "Experimental verification of proton beam monitoring in a human body by use of activity image of positron-emitting nuclei generated by nuclear fragmentation reaction," Radiol. Phys. Technol. **1**(1), 44–54 (2008).

[12]K. Parodi and W. Enghardt, "Potential application of PET in quality assurance of proton therapy," Phys. Med. Biol. **45**, N151–N156 (2000).

[13]K. Parodi, W. Enghardt, and T. Haberer, "In-beam PET measurements of $\beta^+$ radioactivity induced by proton beams," Phys. Med. Biol. **47**, 21–36 (2002).

[14]K. Parodi, F. Ponisch, and W. Enghardt, "Experimental study on the feasibility of in-beam PET for accurate monitoring of proton therapy," IEEE Trans. Nucl. Sci. **52**, 778–786 (2005).

[15]K. Parodi, H. Paganetti, H. A. Shih, S. Michaud, J. S. Loeffler, T. F. Delaney, N. J. Liebsch, J. E. Munzenrider, A. J. Fischman, A. Knopf, and T. Bortfeld, "Patient study of in vivo verification of beam delivery and range, using positron emission tomography and computed tomography imaging after proton therapy," Int. J. Radiat. Oncol., Biol., Phys. **68**(3), 920–934 (2007).

[16]K. Parodi, H. Paganetti, E. Cascio, J. B. Flanz, A. A. Bonab, N. M. Alpert, K. Lohmann, and T. Bortfeld, "PET/CT imaging for treatment verification after proton therapy: A study with plastic phantoms and metallic implants," Med. Phys. **34**(2), 419–435 (2007).

[17]K. Parodi, A. Ferrari, F. Sommerer, and H. Paganetti, "Clinical CT-based calculations of dose and positron emitter distributions in proton therapy using the FLUKA Monte Carlo code," Phys. Med. Biol. **52**, 3369–3387 (2007).

[18]S. Agostinelli *et al.*, "(GEANT4 Collaboration) 2003 GEANT4: a simulation toolkit," Nucl. Instrum. Methods Phys. Res. A **506**, 250–303 (2003).

[19]J. Allison *et al.*, "(GEANT4 Collaboration) 2006 GEANT4 developments and applications," IEEE Trans. Nucl. Sci. **53**, 270–278 (2006).

[20]A. Fassò, A. Ferrari, J. Ranft, and P. Sala, FLUKA-98 (http://www.oecd-nea.org/science/iend.hide/iend_20.pdf) (1998).

[21]F. Ponisch, K. Parodi, B. G. Hasch, and W. Enghardt, "The modelling of positron emitter production and PET imaging during carbon ion therapy," Phys. Med. Biol. **49**, 5217–5232 (2004).

[22]NNDC : http://www.nndc.bnl.gov./

[23]G. Moliere, "Theorie der Streuung schneller geladener Teilchen II," Nucl. Instrum. Methods Phys. Res. B **74**, 467–490 (1948).

[24]L. V. Highland, "Some practical remarks on multiple scattering," Nucl. Instr. Methods **129**, 467–499 (1975).

[25]R. G. Lynch and I. O. Dahl, "Approximations to multiple Coulomb scattering," Nucl. Instrum. Methods Phys. Res. B **58**, 6–10 (1991).

[26]M. Hollmark *et al.*, "Influence of multiple scattering and energy loss straggling on the absorbed dose distributions of therapeutic light ion beams: I. Analytical pencil beam model," Phys. Med. Biol. **49**, 3247–3265 (2004).

[27]N. Kanematsu, "Semi-empirical formulation of multiple scattering for the Gaussian beam model of heavy charged particles stopping in tissue-like matter," Phys. Med. Biol. **54**, N67–N73 (2009).

[28]B. Schaffner and E. Pedroni, "The precision of proton range calculations in proton radiotherapy treatment planning: experimental verification of the relation between CT-HU and proton stopping power," Phys. Med. Biol. **43**, 1579–1592 (1998).

[29]H. Jiang, J. Seco, and H. Paganetti, "Effects of Hounsfield number conversions on patient CT based Monte Carlo proton dose calculation," Med. Phys. **34**, 1439–1449 (2007).

[30]H. Jiang and H. Paganetti, "Adaptation of GEANT4 to Monte Carlo dose calculations based on CT data," Med. Phys. **31**, 2811–2818 (2004).

[31]H. Paganetti, H. Jiang, K. Parodi, R. Slopsema, and M Engelsman, "Clinical implementation of full Monte Carlo dose calculation in proton beam therapy," Phys. Med. Biol. **53**, 4825–4853 (2008).

[32]H. Paganetti, "Dose to water versus dose to medium in proton beam therapy," Phys. Med. Biol. **54**, 4399–4421 (2009).

[33]S. Espana and H. Paganetti, "The impact of uncertainties in the CT conversion algorithm when predicting proton beam ranges in patients from dose and PET-activity distributions," Phys. Med. Biol. **55**, 7557–7571 (2010).

ELSEVIER

Int. J. Radiation Oncology Biol. Phys., Vol. 76, No. 1, pp. 277–286, 2010

0360-3016/10/$–see front matter

doi:10.1016/j.ijrobp.2009.05.065

**PHYSICS CONTRIBUTION**

# THE DEVELOPMENT AND CLINICAL USE OF A BEAM ON-LINE PET SYSTEM MOUNTED ON A ROTATING GANTRY PORT IN PROTON THERAPY

TEIJI NISHIO, PH.D.,*† AYA MIYATAKE, M.SC.,‡ TAKASHI OGINO, M.D.,* KEIICHI NAKAGAWA, M.D.,† NAGAHIRO SAIJO, M.D.,§ AND HIROYASU ESUMI, M.D.||

From the *Particle Therapy Division, Research Center for Innovative Oncology, National Cancer Center, Kashiwa; †Department of Radiology, Graduate School of Medicine, University of Tokyo; ‡Department of Nuclear Engineering and Management, Graduate School of Engineering, University of Tokyo; §Deputy Director, National Cancer Center, Kashiwa; and ||Director, National Cancer Center, Kashiwa

**Purpose: To verify the usefulness of our developed beam ON-LINE positron emission tomography (PET) system mounted on a rotating gantry port (BOLPs-RGp) for dose–volume delivery-guided proton therapy (DGPT).**
**Methods and Materials: In the proton treatment room at our facility, a BOLPs-RGp was constructed so that a planar PET apparatus could be mounted with its field of view covering the iso-center of the beam irradiation system. Activity measurements were performed in 48 patients with tumors of the head and neck, liver, lungs, prostate, and brain. The position and intensity of the activity were measured using the BOLPs-RGp during the 200 s immediately after the proton irradiation.**
**Results: The daily measured activity images acquired by the BOLPs-RGp showed the proton irradiation volume in each patient. Changes in the proton-irradiated volume were indicated by differences between a reference activity image (taken at the first treatment) and the daily activity-images. In the case of head-and-neck treatment, the activity distribution changed in the areas where partial tumor reduction was observed. In the case of liver treatment, it was observed that the washout effect in necrotic tumor cells was slower than in non-necrotic tumor cells.**
**Conclusions: The BOLPs-RGp was developed for the DGPT. The accuracy of proton treatment was evaluated by measuring changes of daily measured activity. Information about the positron-emitting nuclei generated during proton irradiation can be used as a basis for ensuring the high accuracy of irradiation in proton treatment.** © **2010 Elsevier Inc.**

**Dose–volume delivery guided proton therapy (DGPT), Beam ON-LINE PET system on rotating gantry port (BOLPs-RGp), Target nuclear fragment reaction.**

## INTRODUCTION

Proton therapy is a form of radiotherapy that enables the concentration of a dose onto a tumor by the use of a scanned or modulated Bragg peak. Therefore, it is very important to evaluate the proton-irradiated volume accurately.

Recently, to ensure the high accuracy of proton therapy, imaging studies of positron-emitting nuclei that are generated by target nuclear fragment reactions involving incident protons and nuclei from a patient's body have been performed (1–14). The annihilation gamma rays from the positron-emitting nuclei were measured by a positron emission tomography (PET) system (specifically a beam OFF-LINE PET system using commercial PET apparatus or PET-computed tomography [CT] apparatus postirradiation or a beam ON-LINE PET system in a proton treatment room). The beam OFF-LINE PET system using the commercial PET-CT apparatus has the advantage of being able to easily acquire fusion images and the ability to reconstruct three-dimensional images. However, the time required for the movement of the patient to the PET room (10–30 min) and the resulting deterioration of the statistical accuracy of the acquired data are large disadvantages. With the beam ON-LINE PET system, capturing a large view and the acquisition of three-dimensional images are difficult because of geometrical problems caused by the beam direction and the PET apparatus (7, 15, 16).

Reprint requests to: Teiji Nishio, Ph.D., Particle Therapy Division, Research Center for Innovative Oncology, National Cancer Center, Kashiwa 6-5-1 Kashiwano-ha, Kashiwa-shi, Chiba 277-8577, Japan. Tel: (+81) 4-7133-1111; Fax: (+81) 4-7134-7048; E-mail: tnishio@east.ncc.go.jp

Conflict of interest: none.

Supported by Health and Labour Science Research Grants from the Japanese Government.

*Acknowledgment*—The authors would like to thank the staff members of the Proton Radiotherapy Department of the National Cancer Center, Kashiwa for their help and the members of SHI Accelerator Service, Ltd., and Accelerator Engineering, Inc., for operating of the proton apparatus. We also acknowledge T. Okamoto of Hamamatsu Photonics, K. K., T. Tachikawa of Sumitomo Heavy Industries, Ltd., and H. Oka of SGI Japan, Ltd., for their technical support.

Received Jan 6, 2009, and in revised form May 28, 2009. Accepted for publication May 29, 2009.

The ability to take daily PET images with a high statistical accuracy while the patient remains in the proton irradiation room is a large advantage. Besides, availability of a cone beam (CB) CT system or CT apparatus in the irradiation room can offer the possibility of daily and in situ monitoring of the patient's anatomy. A prototype beam ON-LINE PET system (BOLPs) was previously constructed for basic research (10), and verification of the proton-irradiated volume in a patient's body was confirmed using a PET apparatus and a PET-CT apparatus (beam OFF-LINE PET system) (13).

A BOLPs mounted on a rotating gantry port (BOLPs-RGp) was constructed in our proton treatment room. Activity measurement and PET imaging were performed in 48 patients with tumors of the head and neck, liver, lungs, prostate, and brain during proton treatment at our facility. The position and intensity of the activity were measured daily using the BOLPs-RGp immediately after proton irradiation. Using the activity measurement, we were able to confirm whether the proton beam irradiation of the tumor was reproducibly performed during the treatment period. Moreover, changes in the activity distribution were observed as the volume of the tumor changed, and these changes were related to the delivery dose, changes in the body shape and position of the patient, and the physiologic changes. The PET images from the BOLPs-RGp were sufficient to provide high-quality proton treatment.

## METHODS AND MATERIALS

### *Design of a beam ON-LINE PET system mounted on an RGp*

Via the detection of pairs of annihilation gamma rays emitted from the generated radioactive nuclei of a patient's body, the BOLPs-RGp is designed to determine the position and activity of the positron-emitting nuclei generated in patients by proton irradiation. Figure 1 is a picture of the BOLPs-RGp. The BOLPs-RGp was developed as a standardized system for use with proton therapy devices. During proton therapy, the detector heads have many degrees of freedom and the system allows remote control adaptation to each new proton beam condition and a patient's position. As a result, the measurement of the activity distribution is simple.

A planar positron imaging system (Hamamatsu Photonics K. K., Hamamatsu, Japan) (17) was newly arranged for the BOLPs-RGp. In comparison to the system used previously (10), the 24 detector units mounted on each detector head were increased to 36 detector units, and each unit was composed of 11 × 10 arrays of BGO ($Bi_4Ge_3O_{12}$) crystals with a crystal size of 2 × 2 × 20 $mm^3$. Furthermore, the 2,400 crystals were increased to 3,600 crystals. The gap of each unit became 3.3 mm from 11.0 mm for minimizing dead space in the detector. The field of view (FOV) became 164.8 × 167.0 $mm^2$ from 120.8 × 186.8 $mm^2$. The maximum field size is 185.0 × 185.0 $mm^2$ in the rotating gantry port with the BOLPs-RGp. Therefore, the FOV can almost cover each treatment site of the head and neck, liver, lungs, prostate, and brain for a proton treatment in our facility. However, in case of prostate, the depth activity distribution is not measured in the entrance of the incident proton beam. The BOLPs-RGp was mounted on and the center of its detection area was aligned with the iso-center of the rotating gantry in the treatment room of the proton therapy facility at our center. A PET image reconstructed by a back-projection method

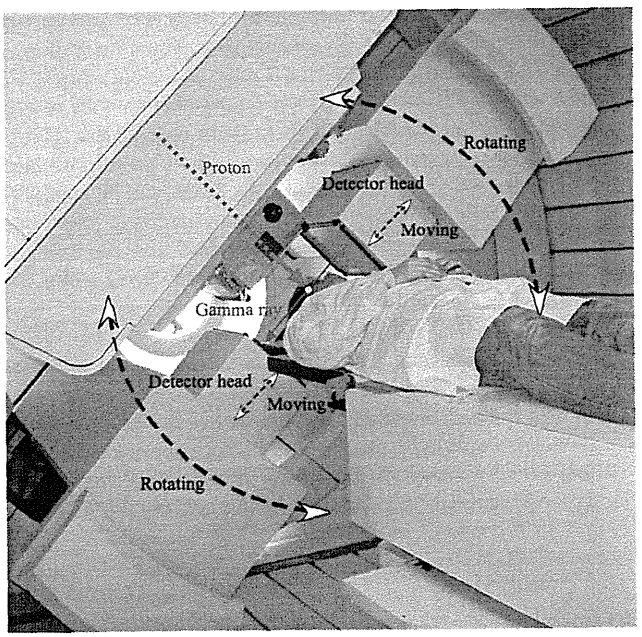


Fig. 1. Setup of the BOLPs-RGp, which is mounted on the rotating gantry port of our proton treatment room.

along the axis of the proton beam direction is always included in the FOV of the opposing detectors together with the axis of the rotating angle of the gantry system. The distance between the two opposing detector heads of the BOLPs-RGp can be adjusted from 30 to 100 cm. When the activity is not being measured, the detector head is stored inside the wall of the gantry device. The position resolution of this system is about 2 mm for the full width at half maximum in the case of use of $^{22}Na$ point source. The maximum data collection rate for the coincident detection of pair annihilation gamma rays is about 4,000 counts/s/$cm^2$ (kcps/$cm^2$). The accuracy of the measurements of activity distribution by this system was verified by a prototype beam ON-LINE PET system (10). The measured data are stored using in the software's list mode format. The activity image is renewed every second. The information of the on-off time points of beam irradiation is recorded in the data, and the image can be restructured according to this information. The PET data from the irradiation field of each patient are managed throughout each treatment day.

The detection efficiency of the distance between the detector heads was calibrated by using the thin-flat acrylic container filled with $^{18}F$-solution. The calibration is used for a correction of the imaging uniformity and the detection sensitivity. The attenuation coefficient of 511-keV gamma rays in the patient's body was calculated by the patient's CT image data. They are used for a construction of the activity imaging. The correction of the photon scattering in the patient's body is not considered for the activity imaging. Furthermore, the photons scattered in the patient's body outside the FOV are detected by the effect of the geometry of the detector head. Therefore, the activity image is contaminated by about 10% background in this system. As the result, the position resolution of the activity distribution will become large more than 2 mm in the clinical case of a proton therapy.

### *Activity measurement in a patient during proton treatment*

The measurement of activity was performed daily in 48 cases involving tumors of the head and neck, liver, lungs, prostate, and brain

using the BOLPs-RGp. The position and intensity of activity were measured during the 200 s immediately after proton irradiation using the trigger signal of the beam-off time. The measurement was performed using the shortest possible distance between the two opposing detector heads of the BOLPs-RGp for each patient. The average distance of the detector heads was 40 cm for the head and neck and the brain, 70 cm for the liver and the lungs, and 50 cm for the prostate. The time of 200 s after proton beam irradiation was chosen according to the intensity of activity estimated from the results of other studies (10, 13). The activity data obtained during proton irradiation were not used for PET imaging. Various types of background radiation (X-rays, gamma rays, and neutrons) occur during proton beam irradiation, and the quality of the activity image becomes markedly worse in their presence (2, 10, 15, 16). Furthermore, high radiation decreases the accuracy of the detector.

Verification of activity measurement was performed in 18, 4, 15, 10, and 1 cases involving tumors of the head and neck, the liver, the lungs, the prostate, and the brain, respectively. The typical fractional dose is 2.5 Gy equivalents (GyE = Gy × the relative biologic effectiveness: [= 1.1 = constant]) for the head and neck, 3.8 GyE for the liver, 4.0 GyE for the lungs, 2.0 GyE for the prostate, and 2.5 GyE for the brain in our facility. The irradiated field is typically planned with three fields in the head and neck and two fields in other sites. Furthermore, the typical number of irradiated field per fractional dose is one in the head and neck, liver, and prostate, and two in the lungs. The fractional dose was delivered over an irradiation time of 10–300 s. The proton beam irradiation was synchronized with the organ motion caused by respiration in the liver and the lungs.

*Procedure for clinical use of activity image*

A flow chart of procedure for clinical use of the BOLPs-RGp is shown in Fig. 2. In the clinical use, the main operation is to take an activity image every day and compare the activity image of the first day of treatment with each activity image during the comparatively long period of the treatment. If the difference of both the images is confirmed by reducing of the tumor size and changing of the body shape, then the new dose distribution is obtained from redose calculation of the plan on a new CT image acquisition, and the first proton treatment plan is immediately corrected to the new plan. As a result, proton treatments of high accuracy can be offered to the patient by keeping of the planned dose delivery.

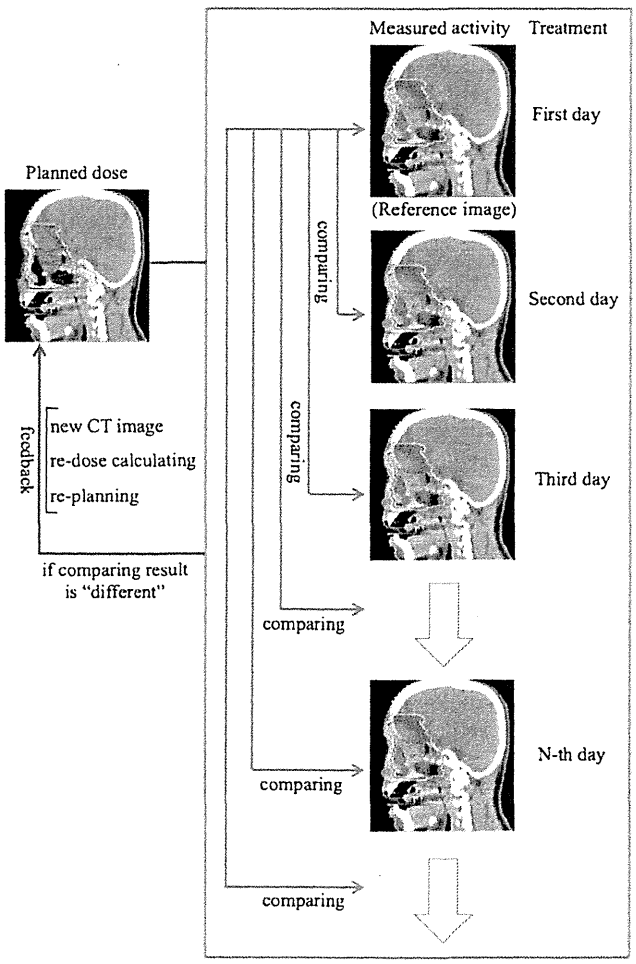


Fig. 2. Flow diagram of the procedure for the clinical use of the BOLPs-RGp.

## RESULTS

*Estimation of the measurement time for PET imaging*

An estimation of an appropriate measurement time for PET imaging was performed using the measured activity data from tumors of the head and neck. The proton beam conditions were as follows: an energy of 120 MeV, a spread out of Bragg peak (SOBP) of 80-mm width, a gantry angle of 340°, a fractional dose of 2.5 GyE, and an irradiation time of 24 s. The distance between the detector heads was 70 cm, and the detection rate of the activity was 1.5 kcps. The left panel of Fig. 3 shows the number of detection events per volume during the detection period after proton beam irradiation. The statistical error (= standard deviation/mean value) decreased as the detection time increased. The error was 2.8% for a 200-s detection time, 3.0% for 150 s, 3.4% for 100 s, and 4.4% for 50 s. The right panel of Fig. 3 shows PET images taken using detection times of (a) 0, (b) 50, (c) 100, and (d) 200 s.

*PET images of each treatment site*

Typical PET images obtained by the BOLPs-RGp are shown for each case involving tumors of the head and neck, the liver, the lungs, the prostate, and the brain. Figure 4 shows the calculated dose distribution and the measured activity distribution on the first treatment day. The beam irradiation parameters were shown in Table 1. The PET images were obtained during the 200 s after proton beam irradiation. The mean detection rates of the activity generated in the proton beam irradiated volume were 1.58, 1.39, 0.53, 1.08, and 1.85 kcps, respectively. The color line and wash normalized to the iso-center show the dose distribution and activity distribution, respectively. By comparing and verifying between the calculated dose distribution and the measured activity distribution, it can be confirmed visually and roughly that the proton beam has irradiated the tumor. In cases of the liver and the lungs, the length of beam irradiation time is adjusted according to the stability of respiration on the treatment day and the patient. By the effect of organ motion, the number of

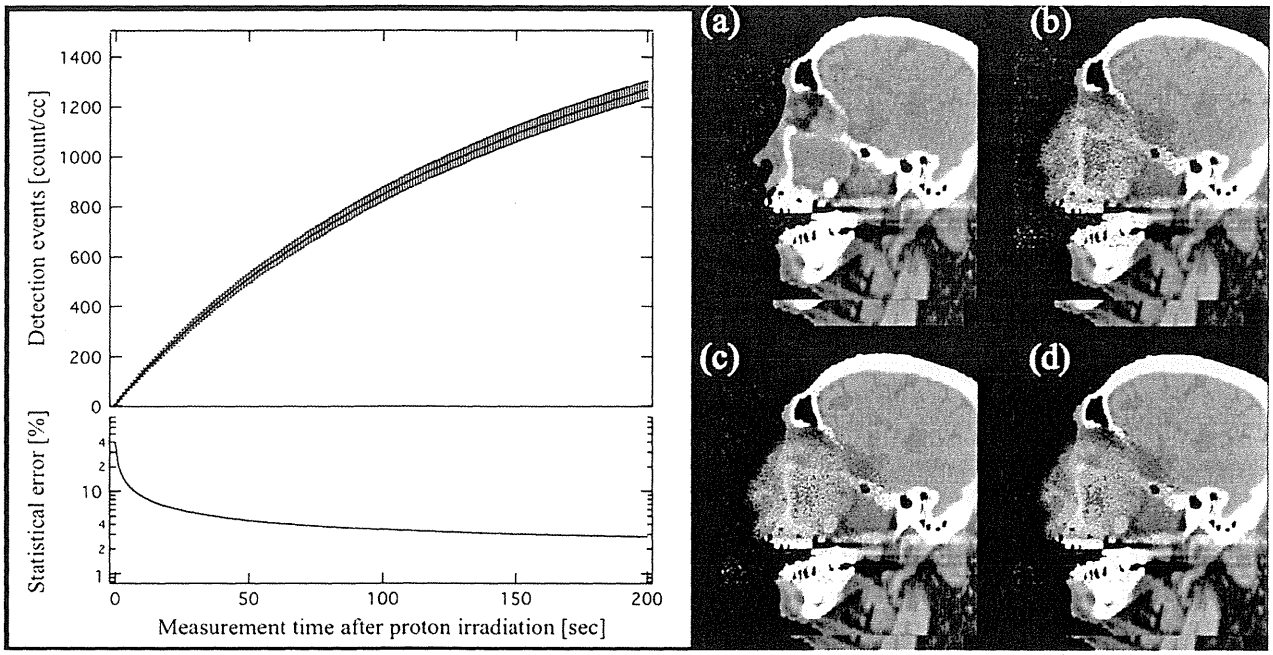


Fig. 3. The number of detection events per volume and PET images obtained during the detection period after proton beam irradiation. The PET images for detection period of (a) 0, (b) 50, (c) 100, and (d) 200 s are shown.

the detection event of the activity measured in the gating window will became about one third of the total detection events, and the statistical error will increase. Therefore, the measurement was performed with no synchronization with organ motion by respiration.

*Changes in the activity distribution during the treatment period*

In each treatment site, the activity distribution changed probably by reduction of the tumor size and changing of the body shape was conspicuously observed in some cases of the head and neck.

The verification was performed for a case involving tumors of the head and neck. Proton beam irradiation was performed in three fields of view: Port 1: 123 MeV, 90-mm SOBP, 350° gantry angle, 0° bed angle; Port 2: 121 MeV, 90-mm SOBP, 10° gantry angle, 20° bed angle; and Port 3: 117 MeV, 80-mm SOBP, 340° gantry angle, 350° bed angle. The irradiation dose was 2.5 GyE. Figure 5 shows a calculated proton dose distribution, an activity distribution, and a depth profile of a 2.5-GyE dose irradiation after a delivery dose of 2.5 (reference image), 10.0, 17.5, or 32.5 GyE from Port 1, a delivery dose of 5.0 (reference image), 12.5, 20.0, or 35.0 GyE, from Port 2, and a delivery dose of 7.5 (reference image), 15.0, 22.5, or 30.0 GyE from Port 3. Changes of the activity distribution were observed according to changes of the proton beam range and the dose delivered by previous irradiations resulted in a reduction of the tumor (see the arrow and the area surrounded by the dotted line in Fig. 5). The changing values of the activity range for each irradiation field (Port 1, Port 2, and Port 3) are shown in upper left of Fig. 6. The activity range was defined by the depth point of 50% distal falloff in the activity distribution normalized at the iso-center. The changing value of the activity range fully exceeded a 10-mm length. Moreover, to observe the changes in the activity distribution in the depth direction in a similar manner, the ratio of the integration of the detected numbers between 20 mm and 70 mm from the iso-center was expressed as follows:

$$R(D) = \frac{\int_{20}^{70} \left(dA(D)/dZ\right) dz}{\int_{20}^{70} \left(dA(0)/dZ\right) dz}. \quad (1)$$

Here, $z$ is the depth, D is the delivery dose, A(D) is the depth activity distribution, and A(0) is the reference depth activity distribution. The ratio of the delivery dose is shown in the middle left of Fig. 6. The bottom left of Fig. 6 is the proton beam irradiation time per fraction dose at each irradiation. The average of the irradiation time was 30 s, and the difference of the irradiation time at random was within 3 s.

In this case, a new CT image was scanned and a retreatment planning was produced after the delivery of 35 GyE of the prescribed dose of 65 GyE. The volume of the tumor was decreased from 184 mL to 125 mL (the arrow in right of Fig. 6 shows the visible tumor reduction), and the maximum beam range was shortened by 20-mm water equivalent length. In the other 2 cases of 18 clinical cases of the head and neck, the changing activity range of more than 10 mm was observed. Similarly, the new CT image acquisition and the retreatment planning were immediately performed after the observation of the changing activity range. The reduction

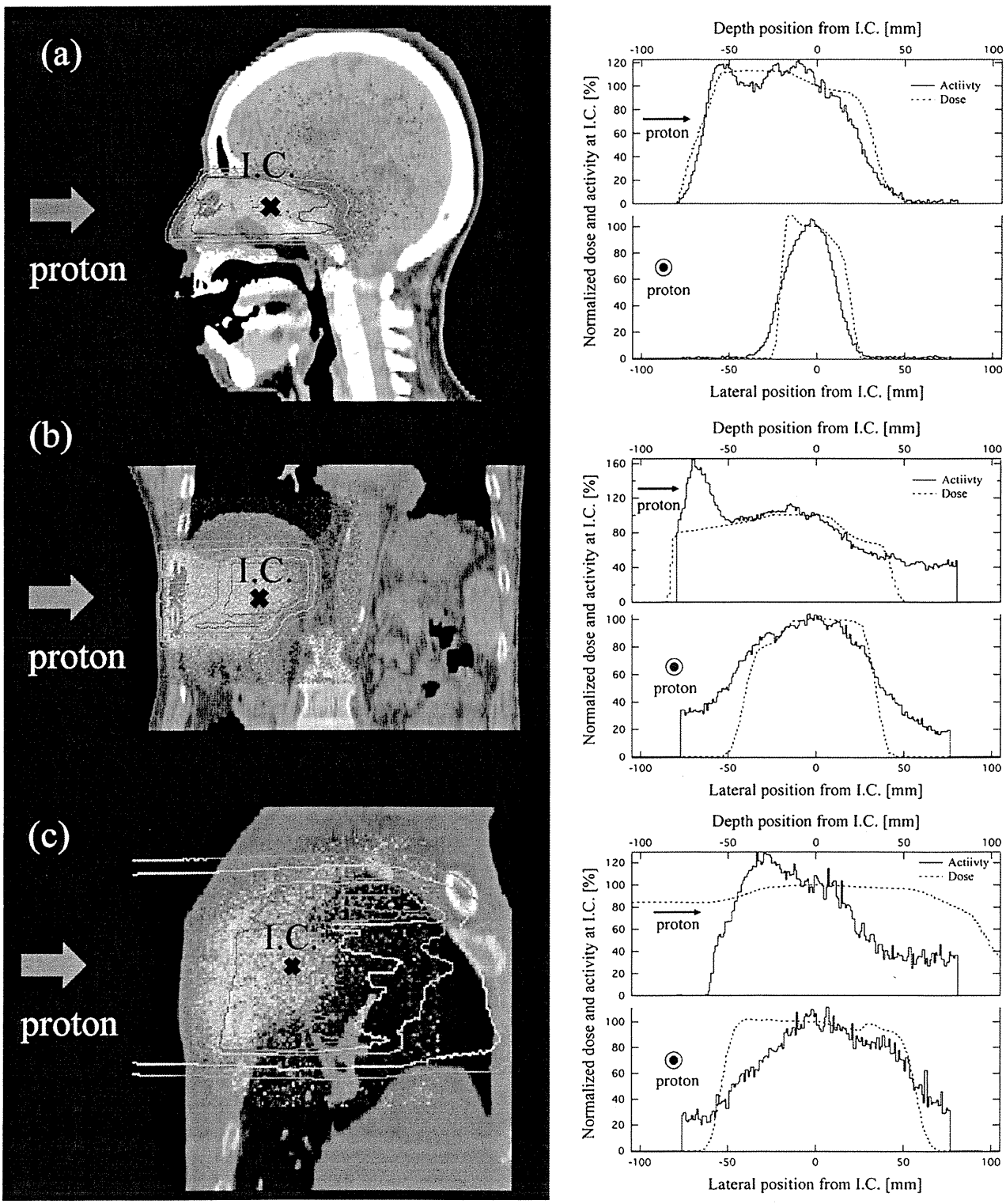


Fig. 4. The calculated dose distribution and the measured activity distribution (left figure), and corresponding lateral and depth profiles (right figure) of the irradiation fields (see Table 1) in each case involving tumors of the head and neck (a), the liver (b), the lungs (c), the prostate (d), and the brain (e), respectively. The iso-dose line of 100% is red, 80% yellowish green, 50% light blue, and 20% purple. The iso-activity wash between 30% and 100% changed from light blue to red.